Journal of Geochemical Exploration 215 (2020) 106546

Contents lists available at ScienceDirect

Journal of Geochemical Exploration

journal homepage: www.elsevier.com/locate/gexplo

# Fluid properties and origins of the Lannigou Carlin-type gold deposit, SW China: Evidence from SHRIMP oxygen isotopes and LA-ICP-MS trace element compositions of hydrothermal quartz

Jun Yan[a,*], John A. Mavrogenes[b], Shen Liu[c], Ian M. Coulson[d]

[a] State Key Laboratory of Ore Deposit Geochemistry, Institute of Geochemistry, Chinese Academy of Sciences, Guiyang 550081, China
[b] Australian National University, Research School of Earth Science, Acton, ACT 2601, Australia
[c] State Key Laboratory of Continental Dynamics and Department of Geology, Northwest University, 229 Taibai Road, Xi'an 710069, China
[d] Solid Earth Studies Laboratory, Department of Geology, University of Regina, Regina, Saskatchewan S4S 0A2, Canada

ARTICLE INFO

*Keywords:*
Lannigou Carlin-type Au deposit
Quartz
LA-ICP-MS trace elements
SHRIMP oxygen isotope
Ore-forming fluid

ABSTRACT

Oxygen isotope and trace elements characteristics of ore-related quartz from Lannigou gold deposit, a typical fault-control second largest Carlin-type Au deposit in SW China, provide valuable information about the properties and origins of the ore-forming fluids. Previous works has focused on vein quartz instead of ore-related jasperoid-like quartz grain due to hard separation. Based upon different cathodoluminescence (CL) textural patterns and intensities observed within the quartz, four generations of quartz from this deposit were identified: Quartz I is sedimentary detrital quartz; Quartz II is *syn*-mineralization jasperoid-like quartz intergrown with and/or containing fine (< 10 μm) As-bearing pyrite and arsenopyrite; Quartz III is late-mineralization veinlet quartz with a small of medium-coarse-grained (about 50–100 μm) As-bearing pyrite; and Quartz IV is the post-mineralization drusy thick-veined quartz. Analyses by sensitive high-resolution ion microprobe (SHRIMP) and laser ablation inductively coupled mass spectrometry (LA-ICP-MS) were used to determine O isotope and trace elements compositions of quartz formed in different stages. The trace elemental (e.g., Al, Li, Ge, Ti) variation of quartz from Quartz II to IV reflect the effects of fluid saturation in $CO_2$ as the result of decarbonization reactions, followed by a progressive fall in $CO_2$, whereas the fluid pH and intensity of argillic alteration increase, progressively. The range of $\delta^{18}O_{VSMOW}$ values in Quartz II (12.1–24.8‰) is wide but narrows in Quartz III (24.1–27.8‰) and IV (24.3–26.9‰). The estimated fluid $\delta^{18}O$ values of early- or main-stage (calculated from Quartz II) is 3.2–15.9‰, the late-stage (calculated from Quartz III) is 12.5–16.2‰, and the post-stage (calculated from Quartz IV) is 9.0–11.5‰. It is suggested that the ore-forming fluids of Lannigou gold deposit reflect a mixed source: a low O isotope end-member that was magmatic- or basement related, whereas the high O isotope end-member may have been fluid interacted with wall-rock, whose influence strengthened during the mineralization episode. The narrow $\delta^{18}O_{VSMOW}$ ranges of Quartz III and IV also suggest that any meteoric water influence on the late hydrothermal system was weak.

## 1. Introduction

Carlin-type gold deposits are primarily found in two main districts: North-Central Nevada (USA) (Arehart, 1996; Dobra, 1997; Hofstra et al., 1999; Hofstra and Cline, 2000; Muntean et al., 2011; Muntean and Cline, 2018) and South China (Hu et al., 2002, 2016, 2017; Su et al., 2008, 2009a, 2009b, 2012). More than 9% of global gold production is provided by Carlin-type gold deposits (Dobra, 1997; Cline et al., 2005). Quartz is a common gangue mineral in this type of deposit, with silicic alteration being an important ore-related alteration style (Cline and Hofstra, 2000; Cline et al., 2005). Ore-related quartz in Carlin-type gold deposits is widely considered to have formed during decarbonatization, when quartz precipitates in the voids left by the dissolution of calcite (Zhang et al., 2003; Cline et al., 2005). Hence, the isotopic character of quartz and any trapped fluid inclusions within this mineral can provide direct constraints on the properties and origin of the ore fluids (Lubben et al., 2012).

Traditionally, bulk quartz from quartz veins formed at a late or post ore depositional stage have been used in the study of Carlin-type gold deposits. However, the generation of quartz closely related to As-

* Corresponding author.
*E-mail address:* yanjun@mail.gyig.ac.cn (J. Yan).

https://doi.org/10.1016/j.gexplo.2020.106546
Received 12 December 2019; Received in revised form 25 March 2020; Accepted 2 April 2020
Available online 21 April 2020

bearing pyrite (*syn*-decarbonatization) has proven difficult to separate, and thus is often ignored (Lubben et al., 2012). Furthermore, studies of the quartz from Carlin-type gold deposits have long focused only on conventional fluid inclusion and H—O isotope analyses. With the advancement of in-situ analytical techniques, especially laser ablation-inductively coupled plasma-mass spectrometry (LA-ICP-MS) and secondary ion mass spectroscopy (SIMS) (Su et al., 2012; Lubben et al., 2012), it is now possible to elucidate detailed information from vein quartz, in terms of both trace element compositions and isotopic character. These data can potentially be used to decipher the source of ore-forming fluids and any property variation in this fluid during mineralization.

In this study, we used cathodoluminescence (CL) techniques to identify anhedral jasperoid-like quartz that is closely inter-grown with As-bearing pyrite from the Carlin-type gold deposit at Lannigou, Southwest China. LA-ICP-MS and sensitive high-resolution ion microprobe (SHRIMP) methods were used to determine the trace elements and oxygen isotope compositions of the different quartz generations, and afterwards based on the new data, the properties and origins of ore-forming fluids were discussed. Since the commonly-used 197 nm laser is not effective in quartz ablation, hampering the analytical quality (Chenery and Cook, 1993), a 157 nm laser ablation was used in this study.

## 2. Geological background

The South China Block is composed of the Yangtze and Cathaysia blocks. It is bordered in the north with the North China Craton and to the west by the Indochina Block. During Triassic continent-continent collision, the Qinling-Dabieshan orogenic belt in the north and the Song Ma suture in the west were formed (Zhou et al., 2006; Wang et al., 2007; Hu and Zhou, 2012; Hu et al., 2017; Fig. 1). The Youjiang basin is situated in the southwestern part of the South China Block, and is mainly controlled by several crustal-scale faults. In this region of China, tectonic activity has resulted in a triangular-shaped basin, which is locally called the “Golden Triangle” (Tu, 1992; Fig. 1). The stratigraphy of this region consists mainly of Cambrian to Triassic carbonate and clastic rocks. There are no exposed granite plutons in the region although intrusions of Triassic and Jurassic ages are inferred to be developed beneath the sedimentary cover(Hu et al., 2002; Peters et al., 2007; Su et al., 2008; Hu and Zhou, 2012; Mao et al., 2013; Pi et al., 2017; Zhu et al., 2017; Fig. 1).

The Lannigou (also called Jinfeng) gold deposit is located on the landward-side sediments of a carbonate platform in the Laizishan anticline in the central of the Golden Triangle. The ore-body (~1500 *m* long by 1200 *m* wide, and 10–50 *m* in thickness) is mainly hosted in fault zones (Fig. 2A). As one of the largest Carlin-type gold deposits in the region, Lannigou deposit has a total Au resource estimated at > 5.3 million Oz, at an average grade of 4.5 g/t Au (Chen et al., 2011). Ore-hosting wall rocks include calcareous siltstone and mudstone of the Xuman and Bianyang formations (Fig. 2B). At the depth of the ore body, there is identified Dachang Formation (or called SBT) (Fig. 2A). The Dachang Formation is widespread across the Youjiang Basin and has a close relationship to low temperature ore deposits (Liu et al., 2017).

The gold in this deposit is mainly hosted in As-bearing pyrite, and gold mineralization is closely related to silicic alteration (Hu et al., 2002; Wang et al., 2003; Zhang et al., 2003; Peters et al., 2007; Chen et al., 2011, 2015a, 2015b; Fig. 3A). The anhedral jasperoid-like quartz grains are closely inter-grown with As-bearing pyrite (Fig. 3E), and it indicated that these jasperoid-like quartz grains are formed during

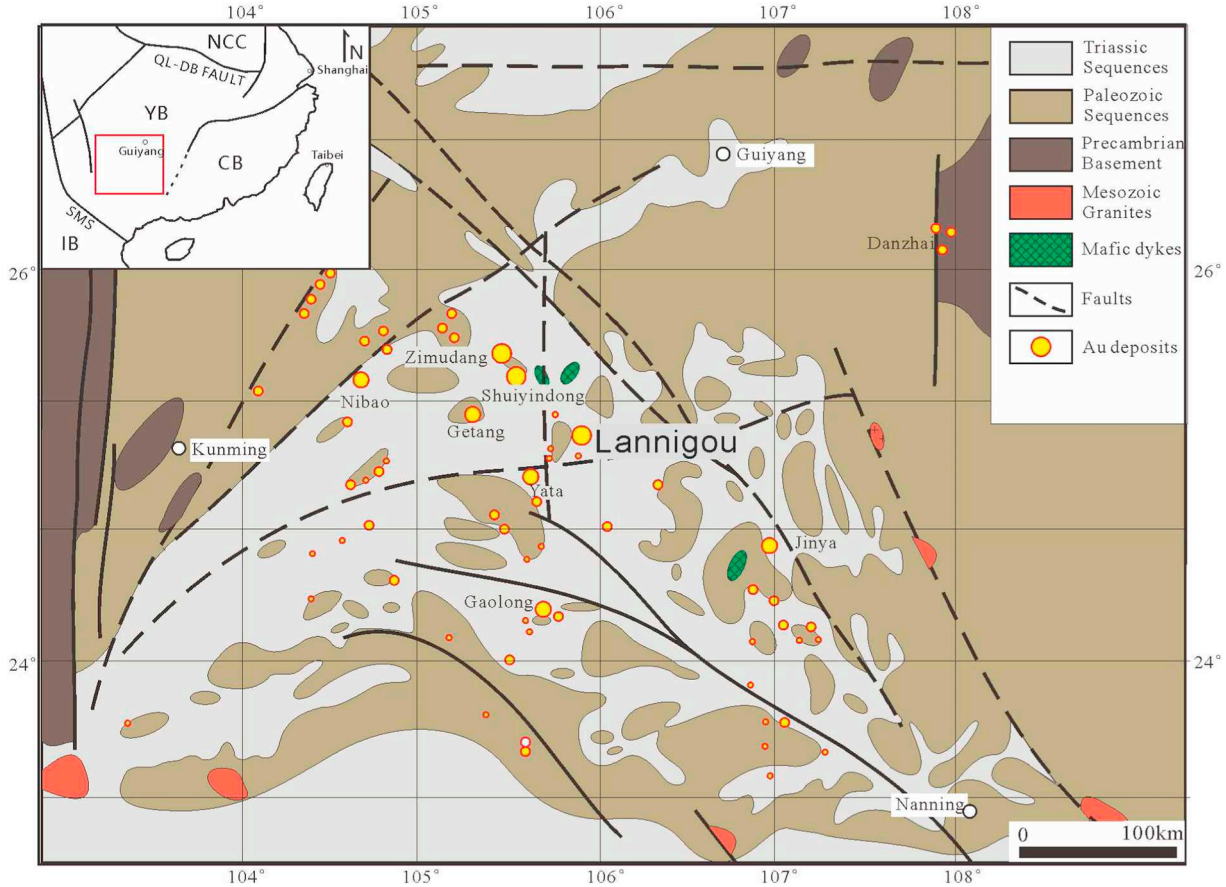


**Fig. 1.** Geological map of Youjiang Basin in SW China (after Hu and Zhou, 2012). IB: Indochina Block, SMS: Song Ma Suture, YB: Yangtze Block, QL-DB: Qinling-Dabie, NCC: North China Craton, CB: Cathaysia Block.

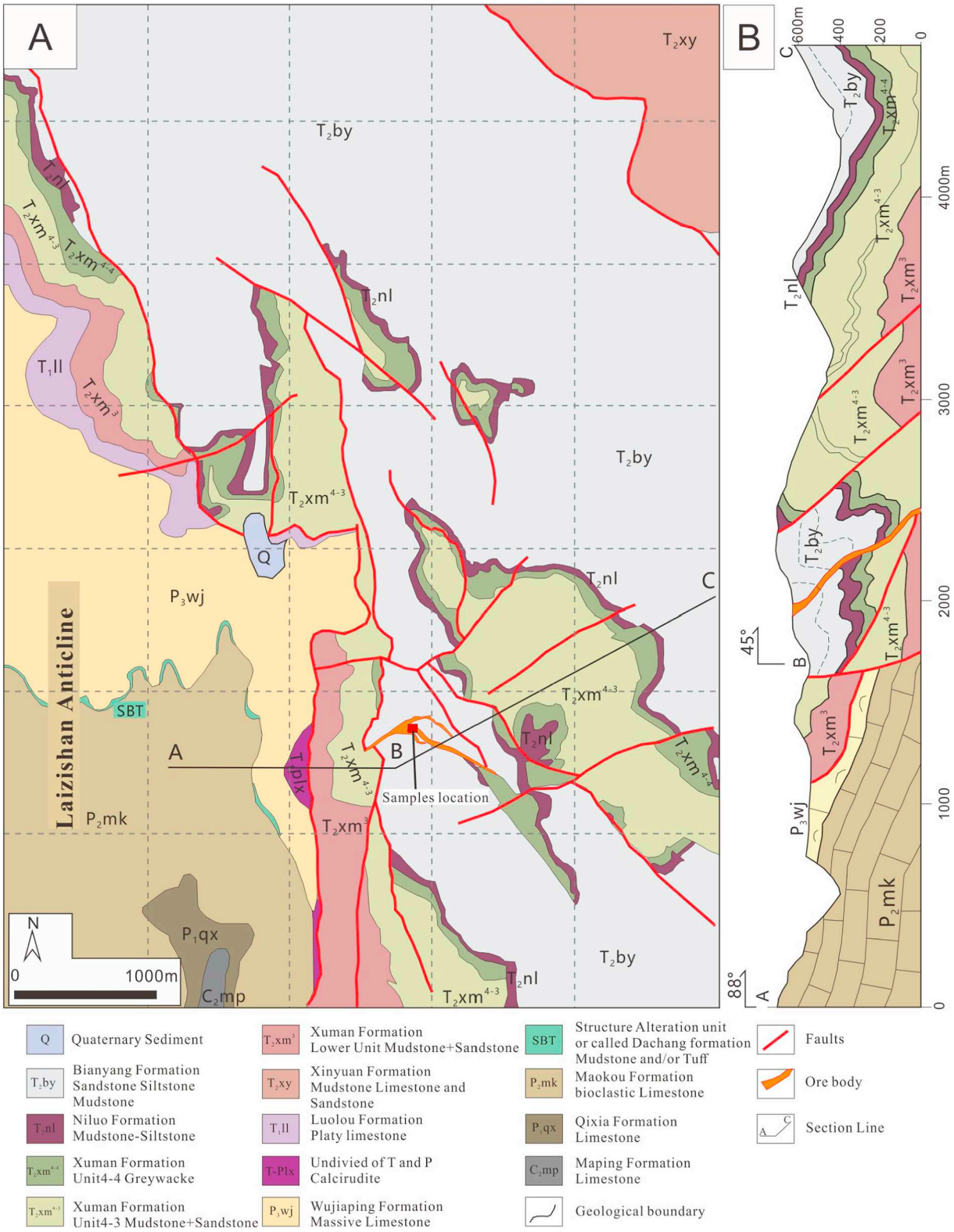


**Fig. 2.** Geology in plane (left) and in A-B-C cross-sectional (right) views of the Lannigou gold deposit (modified after Eldorado Gold Corp. Ltd., 2011). The Au orebody is located on the landward-side of a carbonate platform in the Laizishan anticline and occurs mainly with zones of faulting. Line A-B-C drawn upon the map is the path of the illustrated cross-section. (For interpretation of the references to colour in this figure legend, the reader is referred to the web version of this article.)

mineralization process. However, it is hard to distinguish them from sedimentary detrital quartz grains. Inspired by previous works of quartz (Lubben et al., 2012; Mao et al., 2017), cathodoluminescence (CL) was used to identify them. Hydrothermal alterations also include decarbonatization and argillization (illite) (Hu et al., 2002; Zhang et al., 2003; Su et al., 2018). During decarbonatization, calcite was dissolved and replaced by quartz, releasing Fe to form pyrite (Su et al., 2009a; Fig. 3B). The argillization, characterized by minerals such as illite, is mainly present in the late stage of mineralization (Hu et al., 2002; Zhang et al., 2003; Fig. 3).

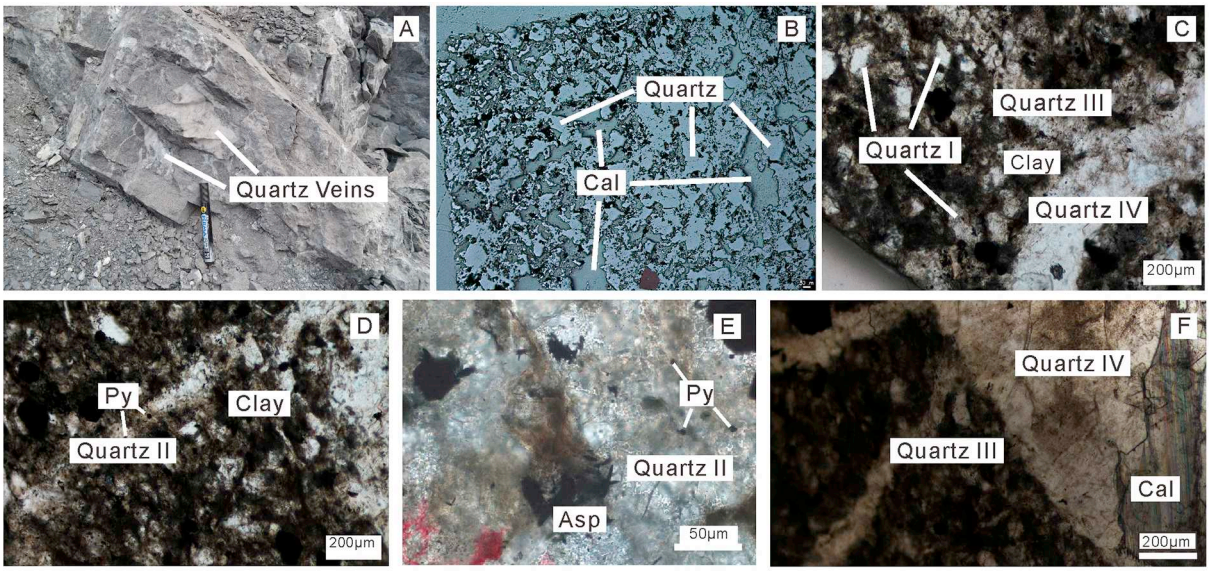


**Fig. 3.** Representative transmitted light photomicrographs of samples from the Lannigou gold deposit. A: representative photo of hand-pick ore sample. B: replacement of calcite and dolomite by jasperoid-like grain quartz during decarbonatization. C-F: Quartz in this sample is divided into four types: Quartz I is detrital quartz and unrelated to mineralization; Quartz II jasperoid-like grain quartz formed during the early or/and main episode of mineralization, and co-exist with arsenopyrite and pyrite; Quartz III veinlet quartz post-dates Quartz II and cross-cuts ore-bearing rock; Quartz IV quartz veins are the latest and usually co-exist with late-stage minerals (e.g., calcite, realgar, stibnite, etc.). Asp = arsenopyrite, Py = pyrite, Cal = calcite, Clay = Clay minerals (illite etc.). (For interpretation of the references to colour in this figure legend, the reader is referred to the web version of this article.)

## 3. Sampling and methods

Eight presentative ore samples with different ore grades were collected from the Lannigou open pit and underground (Fig. 2, Table 1). All the samples were prepared as thin sections. Electron probe micro analysis (EPMA) and CL imaging were performed on each sample to help in the selection of the area of interest for the subsequent SHRIMP and LA-ICP-MS investigation. These areas were then cut into 5 mm slabs and mounted in epoxy (diameter: 1 in.) prior to the analysis.

Quartz CL and back-scattered electron images (BSE) were collected using a JEOL JSM-7800F scanning electron microscope (SEM) fitted with a Gatan MonoCL4 cathodoluminescence system at the National Key Laboratory of Ore Deposit Geochemistry, Institute of Geochemistry, Chinese Academy of Sciences (IGCAS), Guiyang. For each CL image collected, a corresponding back-scattered electron image (BSE) was taken to assess the surface topography and help locate areas for the follow-up analysis. Images were taken with a working distance of about 13 mm and an accelerating voltage of 15 kV.

Major and minor element compositions of the selected quartz generations were determined using an EMPA-1600 microprobe housed at the IGCAS, and under the following operating conditions: 15 kV, 10 nA and a beam size of 10 μm in diameter. The analysis times for major elements were on the order of ~30 s, and slightly longer for minor elements. The content of Al, Si, Ca, Ti, Cr, Mn and Fe in quartz were analyzed as oxides. The detection limits were better than 0.01 w.t. %.

In-situ quartz oxygen isotope analysis was performed at the Research School of Earth Sciences, Australian National University, using a sensitive high-resolution ion microprobe SI (SHRIMP SI). The quartz sample spots were separated into different growth stages according to microscope and CL images, and the analysis spots were identified via secondary electron imaging. The samples are mounted onto epoxy (1-in. mount), and then Al-coated to increase conductivity. A primary ion beam of $Cs^+$ and spot sizes of 20 to 30 μm were used, and the analysis procedures follow that outlined in Ickert et al. (2008). The data obtained were normalized to the quartz oxygen isotope standard NBS-28 (NIST SRM-8546), with its corresponding recommended $V\text{-}_{SMOW}$ value of 9.6‰ (Alexandre et al., 2006). The analytical uncertainty for NBS-28 was 0.5‰, while the sample internal accuracy varied from 0.114‰ to 0.310‰.

After the SHRIMP oxygen isotope analysis, LA-ICP-MS trace element analysis was conducted on or near the SHRIMP analysis spots. The trace element analysis was also performed at the Research School of Earth Sciences, Australian National University, using a 157 nm laser ablation system coupled with a Varian 820-ICPMS. A spot size of 30–50 μm diameter was used, and pre-ablation was carried out to remove the contaminants on the sample surface (e.g., Landtwing and Pettke, 2005; Tanner et al., 2013). It was particularly important in this study to remove any contamination that may have been present from the Al coating applied for the SHRIMP analysis. The analysis conditions include a 10 Hz frequency and 60 s signal collection time. However, only

**Table 1**
Sampling location and details of samples.

| Sample No. | Description | Sampling location |
|---|---|---|
| LNG3-1<br>LNG3-3 | High Au-grade (> 7 g/t) dark gray quartz veined breccia siltstone containing disseminated arsenopyrite | 520 *m* level ore body at open-pit |
| LNG-3-6<br>LNG3-8 | Low Au-grade (1–2 g/t) quartz veined sandstone containing disseminated arsenian-pyrite | 500 *m* level ore body at open-pit |
| LNG3-9<br>LNG3-11<br>LNG3-12 | Quartz veined siltstone containing disseminated arsenopyrite, Au-grade increasing from 4.5 g/t to 6 g/t | 250–370 *m* level at underground (ore heap samples) |
| LNG6-1 | Quartz veined siltstone containing cubic pyrite and calcite breccia | 500 *m* level near ore body with very low Au-grade at open-pit |

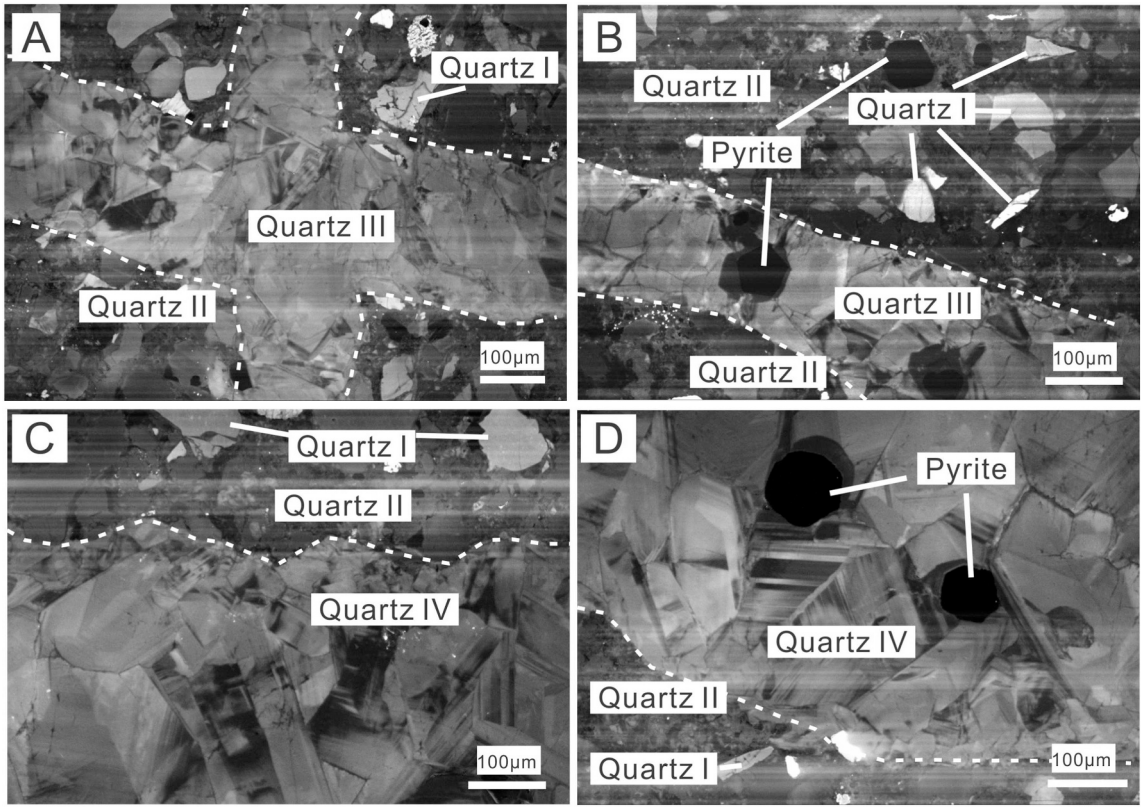


**Fig. 4.** Representative cathodoluminescence images of samples from the Lannigou gold deposit. Quartz I is brightly luminescent and brecciated; Quartz II jasperoid-like grain quartz is weakly luminescent but slightly brighter than the CL of interstitial clay minerals; Quartz III veinlet is brightly luminescent, and lacks zoning; Quartz IV veins contains distinct oscillatory growth zoning. White dot lines are boundary of Quartz III/IV veinlets/veins. (For interpretation of the references to colour in this figure legend, the reader is referred to the web version of this article.)

signal from the first 30 s (or less) were chosen for data processing, in order to avoid potential down-hole fractionation (Tanner et al., 2013) and/or signal fluctuation towards the end of the ablation process. NIST-612 glass was used as a standard, and the data were reduced using Iolite software (Paton et al., 2011).

## 4. Results

### 4.1. Stages of quartz formation

Based on cross-cutting relationships observed in hand samples, under microscopy and from cathodoluminescence features, the quartz samples are divided into four stages during mineralization (Quartz I to IV): (I) sedimentary detrital grain quartz; (II) *syn*-mineralization jasperoid-like grain quartz; (III) veinlet quartz; (IV) drusy thick-veined quartz. These types of quartz can be found in same hand sample. Features of Quartz I to IV are shown in Figs. 3 and 4.

Quartz I detrital grain quartz is unrelated to mineralization. These grains show bright luminescence and distinct angular and/or brecciated features. The diameter of them are usually over 100 μm.

Quartz II jasperoid-like grain quartz is commonly intergrown with and/or contain fine (< 10 μm) As-bearing pyrite and arsenopyrite. This quartz generation is fine-grained (diameter < 100 μm), anhedral, with clay mineral and coarse As-bearing pyrite as common interstitial phases. Under CL imagery, Quartz II grains are weakly luminescent but slightly brighter than the CL of the interstitial clay minerals. According to the CL luminescent, Quartz II can be clearly distinguished from Quartz I.

Quartz III occurs as veinlets (100–500 μm thick) commonly cross-cut the ore-hosting siltstone, and include a small amount of medium to coarse-grained (50–100 μm) As-bearing pyrite. According to the cross-cutting relationship, Quartz III veinlets are later than Quartz II jasperoid-like grain quartz. This quartz is subhedral to euhedral, while the As-bearing pyrite contain typical core-rim patterns of zonation. Under CL imagery, the Quartz III appears brightly luminescent and homogenous, with no distinct oscillatory growth zoning or bands observed.

Quartz IV is present in veins from 200 μm to few cm thick which commonly cross-cut the ore and Quartz III veinlets, and rarely contain As-bearing pyrite. These quartz grains are coarse, euhedral to drusy, and commonly intergrown with calcite. The drusy quartz is chiefly accompanied by realgar, stibnite and cinnabar. Compared to Quartz III, luminescent of Quartz IV is brighter and shows distinct growth zoning.

### 4.2. Geochemical features of quartz

EPMA work was mainly focused on Quartz III and IV veins, and the determined results are shown in Table 2, Fig. 5 and Appendix I. From the results, it is evident that in addition to $SiO_2$, the quartz contains trace to minor amounts of Al ($Al_2O_3$ = 0.01–0.89 w.t.%). The EPMA work also detected minor Fe (FeO up to 0.12 w.t.%), while Ti, Ca, Cr, and Mn contents were near or below the detection limit for this method.

As for the trace element results at determined by LA-ICP-MS (Table 3, Fig. 6; Appendix II), most abundant trace elements found in mineralization-related quartz are Ti, Li, Al and Ge. Elements such as Be, P, K, Cu, Zn and Pb were near or below detection limits, regardless of the quartz generation. Titanium content was relatively low in Quartz III and IV (< 3.0 ppm), but higher in Quartz II (up to few tens of ppm). In contrast, Li content in Quartz II (near or below the detection limit) is lower than that in Quartz III and IV generations (16.5–116.5 ppm; avg. 51.8 ppm). Aluminum content in all 4 different types of quartz were relatively high, and Al increases progressively from Quartz II to IV: Quartz II (9.0–776 ppm), Quartz III (535–1555 ppm), and Quartz IV

**Table 2**
EPMA geochemistry (w.t.%) of the Lannigou quartz veins. N = number of analyzed spots.

| Sample | N | MgO | $Al_2O_3$ | $SiO_2$ | CaO | $TiO_2$ | $Cr_2O_3$ | MnO | FeO | Total |
|---|---|---|---|---|---|---|---|---|---|---|
| LNG3-1 | 27 | < 0.01 | 0.31 | 98.43 | < 0.01 | < 0.01 | < 0.01 | < 0.01 | < 0.01 | 98.78 |
| LNG3-3 | 24 | < 0.01 | 0.37 | 97.78 | < 0.01 | < 0.01 | < 0.01 | < 0.01 | < 0.01 | 98.24 |
| LNG3-8 | 36 | < 0.01 | 0.17 | 99.19 | < 0.01 | < 0.01 | < 0.01 | < 0.01 | < 0.01 | 99.42 |
| LNG3-9 | 32 | < 0.01 | 0.22 | 98.26 | < 0.01 | < 0.01 | < 0.01 | < 0.01 | < 0.01 | 98.61 |
| LNG3-11 | 26 | < 0.01 | 0.2 | 99.02 | < 0.01 | < 0.01 | < 0.01 | < 0.01 | < 0.01 | 99.26 |

(750–2439 ppm). Germanium content was generally low (0.5–6.4 ppm), except for some spots in stage IV quartz (28.8 ppm).

### 4.3. Oxygen isotopes of quartz

In this study, we analyzed six samples selected from various parts of the Lannigou orebody, including the different types of quartz. SHRIMP in-situ oxygen isotope compositions were measured at 90 spots from nine analysis areas in the six samples. Compared to the published data obtained from conventional quartz single-mineral analyses ($\delta^{18}O_{quartz}$ = 22.7–26.1‰, Zhang et al., 2003; Su et al., 2009a), the results of SHRIMP show that the mineralization-related quartz (Quartz II to IV) contains a wide range in oxygen isotope values ($\delta^{18}O_{VSMOW}$ = 12.1–27.8‰). Comparatively, Quartz I has low $\delta^{18}O$ values (8.6–16.8‰). Quartz II shows a wide range of $\delta^{18}O$ values (12.1–24.8‰), whereas the $\delta^{18}O$ of Quartz III and IV are higher and within a relatively narrow range (24.1–27.8‰ and 24.3–26.9‰, respectively) (Table 4, Appendix III; Fig. 7A).

## 5. Discussion

### 5.1. Relation between CL intensity and origins of quartz

The CL intensity of quartz, especially if coupled to trace elements within the quartz, can provide quick insight of different origins of quartz (Coulson, 2014; Rusk, 2014). Previous studies have suggested that the CL intensity of hydrothermal quartz commonly shows a positive correlation with Ti- and/or Al- content (Murray and Bruce, 2007; Rusk et al., 2008; Gotte et al., 2011). For example, the CL brightness (CL emission at the wavelength of ~425–450 nm) has been shown to correlate strongly with increasing Ti-content in some high-temperature deposits (Müller et al., 2003), and with elevated Al content in some low-temperature deposits, though not as strongly as for Ti (Rusk, 2014). In this study, Quartz I shows high CL intensity that match notably higher levels of Ti than for the mineralization-related hydrothermal quartz of Quartz II to IV at Lannigou (Fig. 4). The high-Ti content (> 27 ppm) of Quartz I is suggestive of an igneous origin (Ackerson et al., 2015), and is distinctly different from the hydrothermal quartz of Quartz II-IV.

In this study, the observed CL brightness increase with Al content progressively from the early- to later- stage hydrothermal quartz (Quartz II to IV). This suggests that the CL intensity and Al content of the Lannigou deposit quartz are closely linked. For Quartz IV, the observed alternating bands of bright-dark CL intensity may additionally relate to factors such as growth rate or co-precipitating phase affecting CL brightness (Gotte et al., 2011).

### 5.2. Ore fluid properties revealed by quartz trace element variation

Previous studies have indicated that the common trace elements in quartz, including Ti, Li, Al and Ge, can reflect upon the fluid physico-chemical conditions attending the formation of quartz (Rusk et al.,

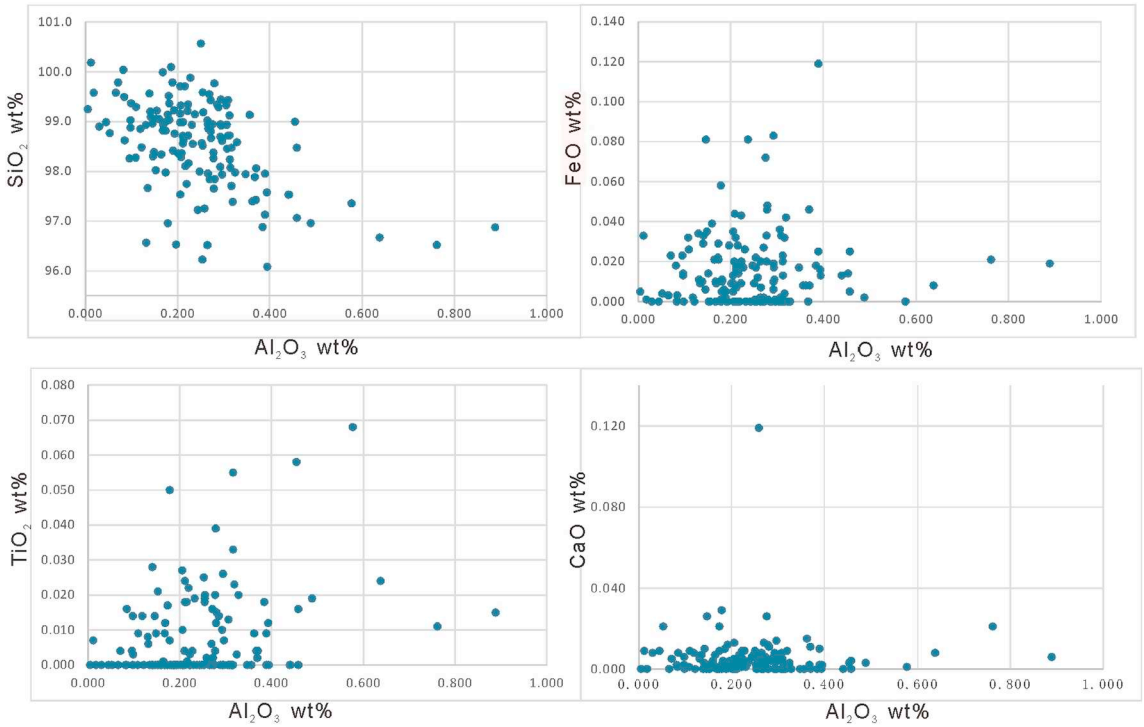


**Fig. 5.** EPMA compositional data for Lannigou quartz; there is a distinct negative correlation observed between $SiO_2$ and $Al_2O_3$., suggestive of Al substituting for Si in the crystal lattice of the quartz. FeO and $TiO_2$ were also detected in trace quantities.

**Table 3**
Average concentration (ppm) of Li, Al, Ti and Ge of different generations of quartz. Detection limits are shown below each element. N = number of analyzed spots.

| | N | Li(ppm) (0.3) | SD(1σ) | Al(ppm) (1.7) | SD(1σ) | Ti(ppm) (1.3) | SD(1σ) | Ge(ppm) (1.0) | SD(1σ) |
|---|---|---|---|---|---|---|---|---|---|
| Quartz I | 11 | 1.2 | 1.2 | 158.7 | 95.1 | 48.9 | 37.7 | 1.6 | 0.4 |
| Quartz II | 10 | 2.9 | 6.1 | 159.5 | 258.3 | 22.0 | 30.5 | 2.2 | 1.4 |
| Quartz III | 13 | 45.1 | 19.2 | 1096.7 | 374.4 | 1.4 | 0.4 | 2.9 | 1.5 |
| Quartz IV | 8 | 62.6 | 24.8 | 1448.1 | 504.2 | 1.7 | 0.5 | 8.5 | 9.6 |

2008; Gotte et al., 2011; Breiter et al., 2013; Audetat et al., 2015). Since the contents of other trace elements in the investigated Lannigou quartz samples are mostly near or below the detection limit, our discussion focuses herein on these four elements. Ti, Li, Al and Ge principally occur in the crystal lattice of quartz in substitution for Si (Gotte et al., 2011; Breiter et al., 2013; Audetat et al., 2015; Mao et al., 2017), and our LA-ICP-MS trace element analysis demonstrates that their contents are markedly different in Quartz II to IV (Fig. 6).

Titanium substitution in quartz is mainly related to temperature of formation of this quartz. Previous studies have shown that Ti content will decrease with temperature dropping (Breiter et al., 2013; Mao et al., 2017). The Ti content of Quartz II is relatively higher compared to Quartz III and IV. Considering the forming sequence from Quartz II to IV, it might reflects a decrease in temperature that accompanied the *syn-* to later-mineralization process. On the other hand, the unusually high Ti contents determined for Quartz II sample (Appendix II, sample 3–11-2-b3 and 3–9-1-b2) may also reflect the existence of a Ti-bearing mineral micro-inclusions (e.g., rutile) within the quartz (Pi et al., 2017).

Aluminum content in quartz is chiefly controlled by the Al content of the precipitating fluid(s), which is, in turn, influenced by the fluid $CO_2$, pH and the elemental equilibrium between any Al-bearing minerals present (e.g., Kaolinite) and this fluid (Rusk et al., 2008; Lehmann et al., 2011). Lehmann et al. suggested that the fluid $CO_2$ content is a more important factor than pH in controlling the fluid Al content, with higher fluid $CO_2$ content leading to lower Al solubility in the fluid. In the Lannigou ore-forming process, the Quartz II and As-bearing pyrite precipitation were coeval with decarbonatization, leading to the replacement of calcite and dolomite by Quartz II jasperoid-like grain quartz (Fig. 3B). The massive $CO_2$ release during decarbonatization may have saturated the ore fluids with $CO_2$, even though the $CO_2$ content is still relatively lower than orogenic deposits. And subsequent to this, the $CO_2$ content likely decreased progressively in the late-/post-mineralization, accompanied by an increase in Al solubility. Besides, the argillic alteration of the wall rocks can introduce more Al into the fluid (from the breakdown of clay minerals, including kaolinite and illite) (Rusk et al., 2008). This might led to a progressive Al increase in the late-stage fluid, which is reflected in the elevated Al contents of later-stage quartz (Quartz III and IV). However, the pH increase attending the ore-forming process does not favor the entry of Al into an ore fluid (Rusk et al., 2008). Previous study has shown that there might be a pH fluctuation of ore-forming fluid caused by fluid mixing during late-ore stage (Yan et al., 2018). As such, the wide Al variation observed (from 535 ppm to 1555 ppm) in Quartz III and IV additionally reflect pH fluctuation within the ore fluids.

From the EPMA results presented above, it can be seen that the Al and Si contents are weakly negatively correlated (Fig. 5). Previous studies have suggested that $Al^{3+}$ in quartz mainly occurs via replacement of $Si^{4+}$ in the crystal lattice (Gotte et al., 2011; Breiter et al., 2013; Audetat et al., 2015). To balance the charge, a concomitant interstitial substitution must also occur of a monovalent cation, such as $Li^+$, or $K^+$ ($Si^{4+} \rightarrow Al^{3+} + Li^+$). That there is a good positive correlation observed between the Al and Li contents in the quartz of all stages adds support to this coupled substitution in the formation of the Lannigou quartz (Fig. 6). While the Ge content of quartz is relatively

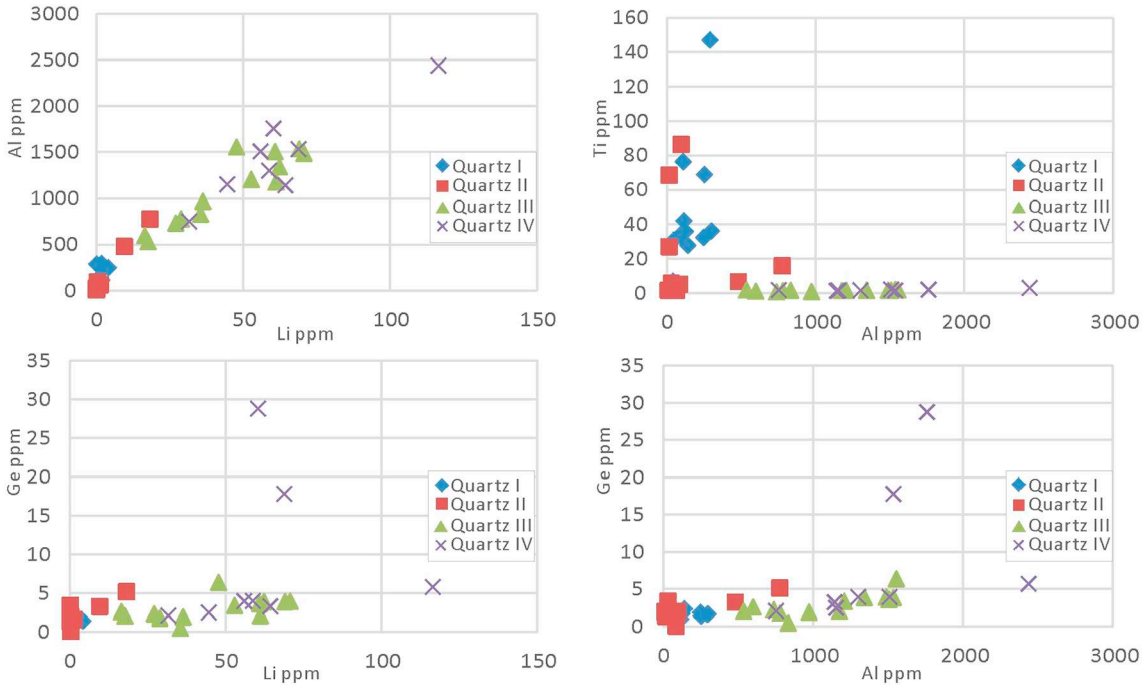


**Fig. 6.** LA-ICP-MS trace element compositions for the various generations of Lannigou quartz. Quartz I detrital quartz is clearly distinct to ore-related quartz (high Ti but low Al, Li). Quartz III and IV have higher Al, Li and Ge but lower Ti content than for Quartz II jasperoid-like grain quartz. Li is positively correlated with Al.

**Table 4**
$\delta^{18}O$ range of different types of quartz by in-situ SHRIMP and estimated O isotope value of fluids. N = number of analyzed spots.

| | N | $\delta^{18}O_{VSMOW}$(quartz)(‰) | Mean | SD(1σ) | $\delta^{18}O_{VSMOW}$(fluid)(‰) | Mean | SD(1σ) | Temperature |
|---|---|---|---|---|---|---|---|---|
| Quartz I | 26 | 8.4–16.8 | 12.6 | 2.5 | | | | |
| Quartz II | 32 | 12.1–24.8 | 17.3 | 3.2 | 3.2–15.9 | 8.4 | 3.2 | 250 °C |
| Quartz III | 22 | 24.1–27.8 | 25.7 | 1.1 | 12.5–16.2 | 14.1 | 1.1 | 200 °C |
| Quartz IV | 16 | 24.3–26.9 | 25.9 | 0.8 | 9.0–11.5 | 10.5 | 0.8 | 150 °C |

low, this element does show weak positive correlations with Al (Fig. 6), and is suggestive that both Al and Ge elements were present in the fluids, potentially deriving through breakdown of the same parent mineral (e.g., Kaolinite; Lehmann et al., 2011).

To summarize, the trace elemental (Al, Li, Ge, and Ti) variation observed within different generations of Lannigou quartz reflects mainly fluid compositional changes occurring throughout the alteration/mineralization process. From Quartz II to IV, the effect of decarbonatization reactions first saturated the ore-forming fluid, which then gradually lost $CO_2$, whereas the fluid pH and intensity of argillic alteration increase, progressively with time. In Quartz III and IV, the wide range of Al content may reflect not only the above changes in $CO_2$, but additionally pH fluctuation of the hydrothermal fluids in these latter stages. The cause of such fluid pH fluctuation might be a late-stage episodic influx of basinal fluids (Yan et al., 2018).

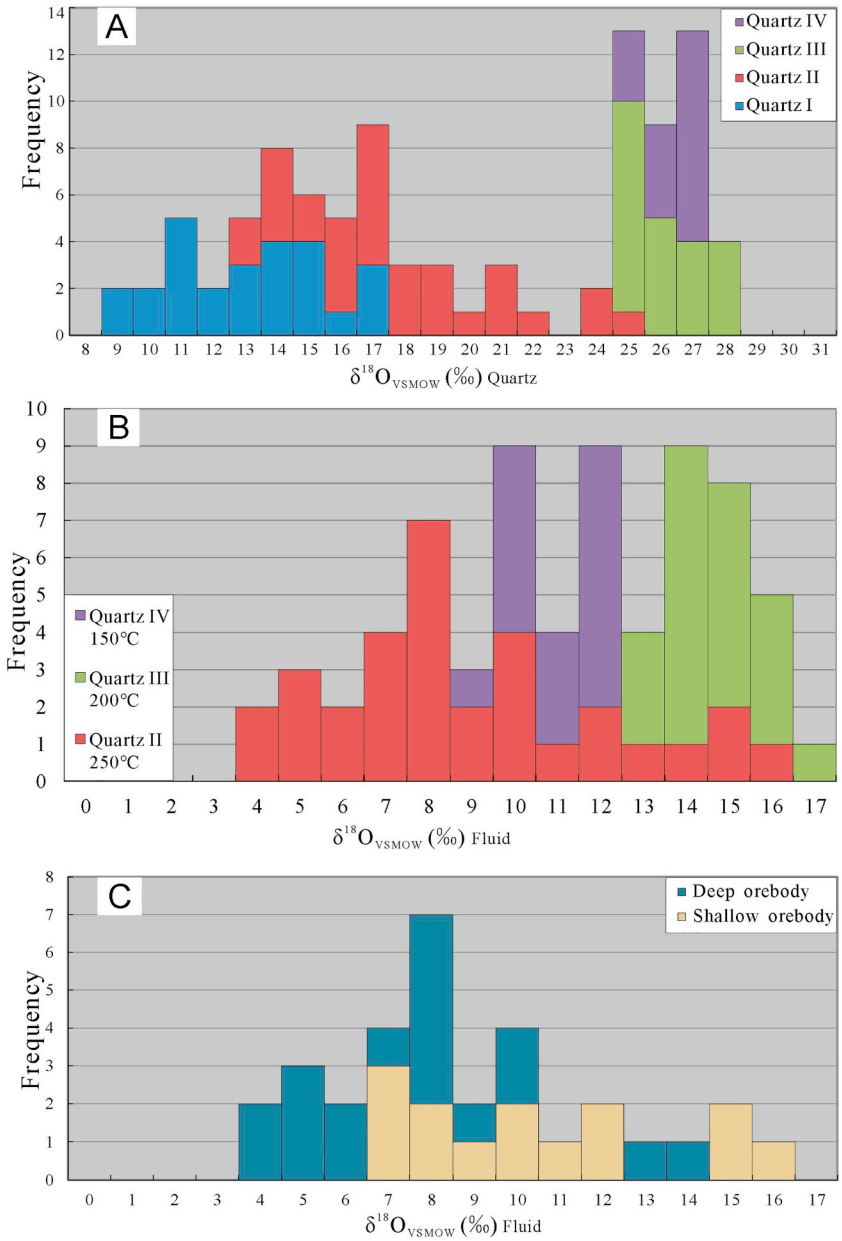


**Fig. 7.** SHRIMP $\delta^{18}O$ values of the various stages of quartz and fluid(s). A: $\delta^{18}O$ for each generation of quartz; the mineralization-related quartz (Quartz II to IV) shows a wide range in $\delta^{18}O$, whereas the $\delta^{18}O$ for vein quartz (Quartz III and IV) is narrow. B: calculated $\delta^{18}O$ of fluid in each mineralization stage. C: different character of fluid $\delta^{18}O$ between the deep and shallow parts of the Lannigou ore body.

### 5.3. Temperature of quartz precipitation and origins of ore-forming fluids

Oxygen isotope compositions of hydrothermal quartz are mainly influenced by temperature and the oxygen isotope compositions of the precipitating fluid. The ore fluid temperature of Carlin-type gold deposit is about 180–240 ˚C in Nevada USA (Cline et al., 2005; Muntean et al., 2011) and 150–250 ˚C ± 50 ˚C in Southwest China (Hu et al., 2002). Using the oxygen isotope fractionation equations for the quartz-water system of Clayton et al. (1972) ($1000\ln\alpha_{QW} = 3.38(10^6\ T^{-2})$ - 3.4) and Matsuhisa et al. (1979) ($1000\ln\alpha_{QW} = 3.34(10^6\ T^{-2})$ - 3.31), a drop in fluid temperatures from 250 ˚C to 150 ˚C, will give a difference in $\delta^{18}O$ value of 6.53‰. Our SHRIMP in-situ $\delta^{18}O$ values for the mineralization-related quartz (i.e., Quartz II to IV) range from12.1‰ to 27.8‰, and this span of values (~15.7‰) is far greater than one that can be influenced by temperature alone. Therefore, fluid temperature fluctuation is unlikely to be the major factor influencing the observed oxygen isotope variation of Lannigou quartz, though it might enlarge the variation range to a certain degree (e.g., for Quartz II).

Carlin-type gold deposit are widely regarded as being moderate to low temperature (300–100 ˚C). In the Lannigou gold deposit, the average homogenization temperature of fluid inclusions are about 250 ˚C, 200 ˚C and 150 ˚C for early, main and late stage ore-fluids respectively (Hu et al., 2002; Zhang et al., 2003). Considering the intergrowth features of quartz and other minerals under optical microscope, we consider that the Quartz II to IV were precipitating at main, later and post stage respectively. And the following temperature of each stage for calculations will be below: 250 ˚C for main stage, 200 ˚C for later stage, and 150 ˚C for post stage. Although the temperatures estimate is not precise for each stage, estimates of the largest range and trend of fluid oxygen isotope value are well constrained.

According to the various formation temperatures of the different-stages of quartz, we estimated oxygen isotope compositions of the ore fluid(s) that were in equilibrium with these quartz. The results suggest that the ore fluids contain $\delta^{18}O$ values of 3.2–16.2‰ (Fig. 7B, Table 3). The fluid $\delta^{18}O$ range of main stage (Quartz II) is relatively wide (3.2–15.9‰). The $\delta^{18}O$ values shows a relatively narrow range of between 12.5 and 16.2‰ for later stage (Quartz III) and between 9.0 and 11.5‰ for post stage (Quartz IV) fluids. Considering the influence of temperature fluctuation, the differences for later and post stage fluids, which are small, suggest that the late- and post-stage hydrothermal system represent a common fluid origin.

Previous work of S isotope for Lannigou gold deposit suggests two end-members of ore fluid (Xie et al., 2018; Yan et al., 2018). The calculated range of fluid $\delta^{18}O$ values for the main stage (Quartz II) fluid also reflects the mixing of two fluids with different $\delta^{18}O$ values, with the fluid from deeper parts of the Lannigou ore-body having lower $\delta^{18}O$ value than for the shallow part (Fig. 7C). It is suggested that one end-member of the mixed fluid has relatively low $\delta^{18}O$ value, representative of the primary ore fluid. These values fall into those typical of magmatic or basement-related fluids $\delta^{18}O$ range (5–8‰). The other fluid end-member has relatively high $\delta^{18}O$ values, and may be sourced from the basinal fluid that had experienced isotopic exchange with wall rocks. Alternatively, the high $\delta^{18}O$ fluid might be the result of water-rock interactions.

Lastly, it is noteworthy that in the Carlin-type gold deposits of Nevada (USA), the oxygen isotope compositions (obtained by bulk-sample or in-situ analyses) show a general lowering of $\delta^{18}O$ with time, which is interpreted to reflect the progressive incursion of meteoric water into the hydrothermal system (Cline et al., 2005; Muntean et al., 2011). Nevertheless, such meteoric water mixing is not prevalent in all Carlin-type gold deposits, for example, Getchell and Turquoise Ridge deposits (Muntean et al., 2011). In a similar way, many typical Carlin-type gold deposits of SW China show typical meteoric water-incursion H—O isotope features (e.g., wide distribute range) in their quartz and kaolinite (Hu et al., 2002; Hofstra et al., 2005; Tan et al., 2015; Hu et al., 2017). At the Lannigou Au deposit, however, evidence from earlier studies of $\delta^{18}O$ for bulk mineral from quartz vein show their relatively high values and narrow range (Zhang et al., 2003). In our study, the $\delta^{18}O$ for Quartz III and IV do not provide evidence for meteoric water influence too. Thus, we consider that any meteoric water influence may have been relatively weak in the gold ore-formation process at the Lannigou deposit.

## 6. Conclusions

Through microscopic observation and CL imaging, we identified CL zoning and intensity features to allow for the characterization of different hydrothermal quartz at Lannigou. We use these data to delineate the unrelated (sedimentary detrital) quartz (Quartz I) from the various stages of mineralization (e.g. *syn*-mineralization jasperoid-like quartz: Quartz II to late and post ore-forming Quartz III and IV). Based upon this subdivision, further analysis of each Lannigou quartz type by in-situ LA-ICP-MS and SHRIMP trace element and oxygen isotope methods yielded the following conclusions:

(1) Trace elements content (Al, Li, Ti and Ge) variation in the Lannigou quartz reflects fluid compositional changes occurring during the alteration and ore-formation processes. Moreover, the progressive increase in Al and Ge indicates the transition from early- to main-stage decarbonatization to late- or post-mineralization argillic alteration. The wide Al content fluctuations observed for Quartz III and IV reflects pH variation caused by incursion of other fluids into the hydrothermal system.
(2) The calculated fluid oxygen isotopes ($\delta^{18}O_{VSMOW}$ = 3.21–16.2‰) reveal that the ore-forming fluids of Lannigou gold deposit have a mixed source. For fluid mixing, a low O-isotope end-member may have been magmatic-hydrothermal or basement related, whereas the high O-isotope end-member was likely basinal fluid, whose influence may have increased with time. The relatively narrow $\delta^{18}O_{VSMOW}$ ranges for Quartz III (12.5–16.2‰) and IV (9.0–11.5‰) vein quartz suggest that meteoric water influence on the latter evolution of the Lannigou hydrothermal system was weak.

## Declaration of competing interest

The authors declare that they have no known competing financial interests or personal relationships that could have appeared to influence the work reported in this paper.

## Acknowledgements

This research was jointly funded by the key project of National Natural Science Foundation of China (41830432), National Natural Science Foundation of China for Youth Scientist (41903044) and the China Postdoctoral Science Foundation (2018M643531). We thank Jinfeng Mine Ltd. for field work support, Dr. Shaohua Dong for assistance with the SEM and CL analyses, and Prof. Li Zhou for assistance with the LA-ICP-MS trace element analyses. The manuscript benefitted from thoughtful reviews and language advancement by two anonymous reviewer, to whom we are grateful.

**Appendix I. Majar and minor elements content of quartz by EPMA (wt%). b.d. = below detect limit**

| Spots no. | MgO | Al2O3 | SiO2 | CaO | TiO2 | Cr2O3 | MnO | FeO | Total |
|---|---|---|---|---|---|---|---|---|---|
| LNG3-1-1011 | b.d. | 0.31 | 98.24 | b.d. | b.d. | b.d. | b.d. | 0.01 | 98.56 |
| LNG3-1-1012 | b.d. | 0.35 | 97.94 | b.d. | b.d. | 0.01 | 0.03 | 0.02 | 98.34 |
| LNG3-1-1013 | 0.01 | 0.3 | 97.93 | 0.01 | 0.01 | 0.03 | b.d. | b.d. | 98.28 |
| LNG3-1-1014 | b.d. | 0.21 | 98.28 | b.d. | b.d. | b.d. | b.d. | 0.02 | 98.51 |
| LNG3-1-1031 | 0.01 | 0.29 | 99.29 | 0.01 | b.d. | 0.01 | 0.01 | b.d. | 99.61 |
| LNG3-1-1032 | b.d. | 0.29 | 99.44 | b.d. | b.d. | 0.02 | b.d. | 0.02 | 99.78 |
| LNG3-1-1033 | b.d. | 0.32 | 98.07 | b.d. | b.d. | b.d. | b.d. | b.d. | 98.38 |
| LNG3-1-2011 | 0.01 | 0.89 | 96.87 | 0.01 | 0.02 | 0.01 | 0.01 | 0.02 | 97.83 |
| LNG3-1-2011-2 | b.d. | 0.32 | 98.47 | b.d. | b.d. | b.d. | b.d. | 0.03 | 98.82 |
| LNG3-1-2012 | 0.01 | 0.3 | 98.61 | b.d. | b.d. | 0.01 | 0.01 | b.d. | 98.94 |
| LNG3-1-2013 | 0.01 | 0.29 | 98.94 | b.d. | 0.01 | b.d. | b.d. | 0.02 | 99.27 |
| LNG3-1-2014 | 0.02 | 0.23 | 98.55 | b.d. | 0.02 | b.d. | b.d. | b.d. | 98.82 |
| LNG3-1-2015 | b.d. | 0.3 | 98.92 | 0.01 | 0.03 | b.d. | b.d. | 0.01 | 99.25 |
| LNG3-1-2021 | b.d. | 0.37 | 97.88 | b.d. | b.d. | b.d. | b.d. | b.d. | 98.25 |
| LNG3-1-2022 | b.d. | 0.12 | 98.48 | b.d. | b.d. | 0.01 | b.d. | b.d. | 98.61 |
| LNG3-1-2023 | b.d. | 0.29 | 98.09 | 0.01 | b.d. | b.d. | 0.02 | 0.01 | 98.41 |
| LNG3-1-2024 | b.d. | 0.31 | 98.45 | 0.01 | b.d. | b.d. | 0.01 | b.d. | 98.78 |
| LNG3-1-3021 | b.d. | 0.39 | 97.13 | b.d. | b.d. | 0.02 | b.d. | 0.12 | 97.65 |
| LNG3-1-3022 | b.d. | 0.31 | 98.72 | b.d. | b.d. | b.d. | b.d. | 0.02 | 99.05 |
| LNG3-1-3023 | b.d. | 0.32 | 97.7 | b.d. | 0.06 | b.d. | 0.01 | b.d. | 98.09 |
| LNG3-1-3024 | b.d. | 0.33 | 97.97 | b.d. | b.d. | b.d. | 0.02 | b.d. | 98.32 |
| LNG3-1-3031 | b.d. | 0.45 | 99 | b.d. | 0.06 | 0.01 | b.d. | 0.01 | 99.53 |
| LNG3-1-3032 | b.d. | 0.18 | 99.51 | b.d. | b.d. | 0.02 | b.d. | 0.01 | 99.71 |
| LNG3-1-3033 | b.d. | 0.31 | 99.33 | b.d. | b.d. | b.d. | 0.01 | b.d. | 99.65 |
| LNG3-1-4011 | 0.02 | 0.27 | 98.8 | b.d. | b.d. | 0.03 | b.d. | 0.03 | 99.16 |
| LNG3-1-4012 | 0.01 | 0.21 | 98.62 | b.d. | 0.02 | 0.01 | b.d. | 0.01 | 98.88 |
| LNG3-1-4013 | 0.01 | 0.14 | 97.66 | 0.01 | b.d. | 0.02 | b.d. | 0.01 | 97.84 |
| LNG3-3-1011 | b.d. | 0.11 | 98.27 | b.d. | b.d. | b.d. | b.d. | 0.03 | 98.41 |
| LNG3-3-1012 | b.d. | 0.39 | 97.95 | 0.01 | 0.01 | 0.04 | b.d. | 0.03 | 98.42 |
| LNG3-3-1013 | b.d. | 0.32 | 97.7 | b.d. | 0.03 | 0.01 | b.d. | b.d. | 98.06 |
| LNG3-3-1014 | b.d. | 0.46 | 98.47 | b.d. | b.d. | 0.01 | 0.01 | 0.03 | 98.97 |
| LNG3-3-1021 | 0.01 | 0.46 | 97.06 | b.d. | 0.02 | b.d. | 0.01 | 0.01 | 97.56 |
| LNG3-3-1022 | b.d. | 0.39 | 97.57 | b.d. | 0.01 | 0.02 | b.d. | 0.02 | 98.01 |
| LNG3-3-1023 | 0.01 | 0.2 | 98.36 | b.d. | b.d. | b.d. | b.d. | 0.01 | 98.58 |
| LNG3-3-1024 | 0.03 | 0.39 | 96.88 | b.d. | 0.02 | 0.03 | 0.02 | 0.02 | 97.38 |
| LNG3-3-1031 | b.d. | 0.33 | 98.58 | b.d. | 0.02 | 0.03 | b.d. | b.d. | 98.96 |
| LNG3-3-1032 | b.d. | 0.19 | 98.42 | b.d. | b.d. | b.d. | b.d. | 0.01 | 98.61 |
| LNG3-3-1033 | 0.01 | 0.36 | 97.39 | 0.02 | 0.01 | b.d. | 0.01 | 0.01 | 97.81 |
| LNG3-3-4011 | b.d. | 0.31 | 98.93 | b.d. | 0.01 | b.d. | 0.03 | 0.04 | 99.32 |
| LNG3-3-4012 | b.d. | 0.37 | 97.42 | 0.01 | b.d. | b.d. | b.d. | 0.05 | 97.86 |
| LNG3-3-4013 | b.d. | 0.31 | 98.71 | 0.01 | b.d. | 0.01 | b.d. | b.d. | 99.03 |
| LNG3-3-4014 | b.d. | 0.64 | 96.67 | 0.01 | 0.02 | 0.03 | b.d. | 0.01 | 97.37 |
| LNG3-3-4021 | b.d. | 0.22 | 98.16 | 0.01 | b.d. | b.d. | b.d. | 0.02 | 98.41 |
| LNG3-3-4022 | b.d. | 0.31 | 99.43 | b.d. | b.d. | 0.02 | b.d. | 0.03 | 99.79 |
| LNG3-3-4023 | b.d. | 0.27 | 98.94 | 0.01 | b.d. | b.d. | b.d. | b.d. | 99.21 |
| LNG3-3-4024 | b.d. | 0.28 | 97.84 | 0.01 | 0.02 | 0.01 | b.d. | b.d. | 98.16 |
| LNG3-3-4025 | b.d. | 0.49 | 96.96 | b.d. | 0.02 | b.d. | b.d. | b.d. | 97.46 |
| LNG3-3-4031 | 0.02 | 0.18 | 96.95 | 0.03 | 0.05 | 0.63 | 0.01 | 0.06 | 97.93 |
| LNG3-3-4032 | b.d. | 0.44 | 97.53 | b.d. | b.d. | b.d. | 0.01 | 0.01 | 97.99 |
| LNG3-3-4033 | 0.01 | 0.58 | 97.35 | b.d. | 0.07 | 0.01 | 0.03 | b.d. | 98.04 |
| LNG3-3-4034 | 0.01 | 0.76 | 96.52 | 0.02 | 0.01 | b.d. | b.d. | 0.02 | 97.34 |
| LNG3-8-1021 | b.d. | 0.27 | 96.51 | b.d. | b.d. | 0.02 | b.d. | b.d. | 96.8 |
| LNG3-8-1022 | b.d. | 0.24 | 97.22 | 0.01 | b.d. | b.d. | b.d. | b.d. | 97.47 |
| LNG3-8-1023 | b.d. | 0.21 | 98.71 | b.d. | 0.02 | b.d. | 0.01 | b.d. | 98.96 |
| LNG3-8-1024 | 0.01 | 0.23 | 98.93 | b.d. | b.d. | 0.02 | b.d. | 0.03 | 99.22 |
| LNG3-8-1011 | b.d. | 0.28 | 98.26 | 0.01 | 0.02 | 0.06 | 0.01 | 0.02 | 98.66 |
| LNG3-8-1012 | 0.01 | 0.05 | 98.99 | 0.01 | b.d. | b.d. | 0.01 | b.d. | 99.06 |
| LNG3-8-1013 | b.d. | 0.15 | 98.96 | b.d. | 0.01 | 0.03 | b.d. | 0.01 | 99.16 |
| LNG3-8-1014 | b.d. | 0.24 | 99.14 | b.d. | b.d. | 0.01 | 0.01 | 0.08 | 99.49 |
| LNG3-8-1015 | b.d. | 0.28 | 98.38 | b.d. | b.d. | 0.02 | b.d. | 0.03 | 98.71 |
| LNG3-8-1016 | b.d. | 0.21 | 98.98 | 0.01 | b.d. | 0.01 | b.d. | 0.01 | 99.21 |
| LNG3-8-2011 | b.d. | 0.22 | 99.34 | b.d. | b.d. | 0.03 | b.d. | 0.01 | 99.61 |
| LNG3-8-2012 | b.d. | 0.08 | 99.49 | b.d. | b.d. | 0.02 | b.d. | b.d. | 99.6 |
| LNG3-8-2013 | 0.11 | 0.26 | 97.25 | 0.12 | b.d. | 0.5 | b.d. | 0.01 | 98.24 |
| LNG3-8-2014 | 0.01 | 0.26 | 99.18 | b.d. | 0.02 | b.d. | b.d. | b.d. | 99.47 |
| LNG3-8-2021 | b.d. | 0.26 | 99.59 | b.d. | 0.02 | 0.01 | 0.01 | 0.02 | 99.89 |
| LNG3-8-2022 | b.d. | 0.21 | 99.32 | b.d. | 0.01 | 0.01 | b.d. | b.d. | 99.54 |
| LNG3-8-2023 | b.d. | 0.19 | 100.09 | 0.01 | b.d. | 0.01 | b.d. | 0.01 | 100.3 |
| LNG3-8-2024 | b.d. | 0.18 | 99.02 | b.d. | b.d. | 0.02 | 0.01 | b.d. | 99.23 |
| LNG3-8-2031 | b.d. | 0.01 | 99.24 | b.d. | b.d. | b.d. | 0.02 | 0.01 | 99.27 |
| LNG3-8-2032 | b.d. | 0.21 | 98.99 | b.d. | b.d. | 0.01 | b.d. | 0.02 | 99.23 |
| LNG3-8-2033 | b.d. | 0.21 | 99.71 | b.d. | b.d. | b.d. | b.d. | 0.01 | 99.92 |
| LNG3-8-2034 | b.d. | 0.1 | 99.37 | b.d. | b.d. | 0.02 | b.d. | b.d. | 99.48 |
| LNG3-8-3021 | b.d. | 0.09 | 98.62 | 0.01 | 0.02 | 0.01 | 0.01 | b.d. | 98.75 |
| LNG3-8-3022 | b.d. | 0.08 | 100.04 | b.d. | b.d. | 0.01 | b.d. | 0.02 | 100.14 |

| | | | | | | | | | |
|---|---|---|---|---|---|---|---|---|---|
| LNG3-8-3023 | b.d. | 0.16 | 99.22 | b.d. | b.d. | b.d. | 0.01 | b.d. | 99.38 |
| LNG3-8-3024 | b.d. | 0.23 | 99.88 | 0.01 | b.d. | 0.07 | b.d. | 0.02 | 100.2 |
| LNG3-8-3041 | 0.01 | 0.03 | 98.9 | 0.01 | b.d. | 0.01 | b.d. | b.d. | 98.95 |
| LNG3-8-3042 | b.d. | 0.18 | 99.36 | b.d. | b.d. | 0.02 | b.d. | 0.01 | 99.59 |
| LNG3-8-3043 | b.d. | 0.19 | 99.78 | b.d. | b.d. | b.d. | b.d. | b.d. | 99.98 |
| LNG3-8-3044 | b.d. | 0.22 | 99.7 | b.d. | 0.02 | b.d. | b.d. | 0.03 | 99.97 |
| LNG3-8-4011 | b.d. | 0.14 | 99.56 | b.d. | b.d. | 0.01 | b.d. | 0.01 | 99.72 |
| LNG3-8-4012 | 0.01 | 0.17 | 98.98 | b.d. | b.d. | b.d. | b.d. | 0.02 | 99.18 |
| LNG3-8-4013 | b.d. | 0.02 | 99.58 | b.d. | b.d. | 0.01 | b.d. | b.d. | 99.6 |
| LNG3-8-4014 | 0.01 | 0.17 | 99.99 | b.d. | 0.01 | b.d. | 0.01 | b.d. | 100.18 |
| LNG3-8-4015 | b.d. | 0.15 | 98.02 | b.d. | 0.02 | 0.01 | b.d. | b.d. | 98.2 |
| LNG3-8-4016 | b.d. | 0.07 | 99.58 | b.d. | b.d. | 0.03 | b.d. | b.d. | 99.67 |
| LNG3-9-1011 | b.d. | 0.12 | 98.85 | 0.01 | 0.01 | b.d. | 0.01 | b.d. | 99 |
| LNG3-9-1012 | 0.01 | 0.19 | 99.23 | 0.01 | b.d. | b.d. | b.d. | b.d. | 99.44 |
| LNG3-9-1013 | 0.01 | 0.21 | 99.16 | 0.01 | b.d. | 0.03 | b.d. | 0.04 | 99.44 |
| LNG3-9-1021 | b.d. | 0.13 | 98.93 | 0.01 | 0.01 | 0.01 | b.d. | 0.03 | 99.12 |
| LNG3-9-1022 | b.d. | 0.16 | 99.05 | b.d. | 0 | b.d. | b.d. | 0.04 | 99.26 |
| LNG3-9-2011 | b.d. | 0.28 | 97.65 | b.d. | 0.04 | b.d. | b.d. | 0.05 | 98.02 |
| LNG3-9-2012 | b.d. | 0.21 | 98.36 | b.d. | b.d. | b.d. | b.d. | 0.04 | 98.61 |
| LNG3-9-2013 | b.d. | 0.28 | 98.94 | 0.03 | b.d. | b.d. | b.d. | 0.07 | 99.32 |
| LNG3-9-2021 | b.d. | 0.17 | 98.81 | 0.01 | b.d. | 0.01 | 0.01 | 0.03 | 99.04 |
| LNG3-9-2022 | b.d. | 0.15 | 99.05 | b.d. | b.d. | 0.02 | b.d. | 0.01 | 99.23 |
| LNG3-9-2023 | b.d. | 0.22 | 99.21 | b.d. | b.d. | b.d. | 0.02 | 0.01 | 99.46 |
| LNG3-9-3011 | 0.01 | 0.26 | 98.51 | 0.01 | 0.02 | b.d. | 0.01 | 0.02 | 98.83 |
| LNG3-9-3012 | b.d. | 0.28 | 99.77 | b.d. | 0.01 | 0.01 | 0.01 | 0.05 | 100.13 |
| LNG3-9-3013 | 0.01 | 0.18 | 99.03 | b.d. | b.d. | 0.01 | b.d. | 0.01 | 99.24 |
| LNG3-9-3014 | b.d. | 0.27 | 97.96 | b.d. | b.d. | b.d. | 0.01 | 0.01 | 98.24 |
| LNG3-9-4011 | 0.01 | 0.1 | 98.88 | 0.01 | 0.01 | 0.02 | b.d. | 0.01 | 99.03 |
| LNG3-9-4012 | b.d. | 0.15 | 98.3 | 0.03 | b.d. | 0.01 | b.d. | 0.08 | 98.57 |
| LNG3-9-4013 | b.d. | 0.27 | 97.84 | 0.01 | 0.01 | b.d. | b.d. | b.d. | 98.13 |
| LNG3-9-4014 | b.d. | 0.1 | 99.02 | b.d. | b.d. | b.d. | b.d. | 0.01 | 99.14 |
| LNG3-9-4015 | b.d. | 0.13 | 96.56 | 0.01 | 0.01 | b.d. | 0.01 | 0.01 | 96.73 |
| LNG3-9-4016 | 0.02 | 0.25 | 96.23 | b.d. | b.d. | b.d. | b.d. | b.d. | 96.5 |
| LNG3-9-4017 | b.d. | 0.2 | 96.53 | b.d. | b.d. | 0.02 | 0.01 | 0.03 | 96.78 |
| LNG3-9-5011 | b.d. | 0.25 | 97.99 | 0.01 | b.d. | 0.01 | 0.01 | 0.02 | 98.29 |
| LNG3-9-5012 | 0.03 | 0.22 | 98.72 | 0.01 | b.d. | 0.02 | 0.01 | 0.04 | 99.05 |
| LNG3-9-5013 | 0.01 | 0.32 | 97.38 | 0.01 | 0.02 | b.d. | 0.01 | 0.04 | 97.8 |
| LNG3-9-5014 | b.d. | 0.21 | 98.71 | b.d. | b.d. | b.d. | b.d. | 0.03 | 98.95 |
| LNG3-9-5015 | b.d. | 0.37 | 98.06 | b.d. | b.d. | b.d. | 0.01 | 0.01 | 98.45 |
| LNG3-9-5016 | b.d. | 0.4 | 96.08 | b.d. | b.d. | 0.39 | 0.02 | 0.01 | 98.89 |
| LNG3-9-5021 | b.d. | 0.17 | 97.97 | 0.02 | 0.02 | b.d. | b.d. | 0.02 | 98.21 |
| LNG3-9-5022 | 0.01 | 0.21 | 97.53 | b.d. | 0.03 | 0.02 | 0.01 | 0.01 | 97.82 |
| LNG3-9-5023 | b.d. | 0.22 | 98.1 | 0.01 | b.d. | b.d. | b.d. | 0.01 | 98.34 |
| LNG3-9-5024 | b.d. | 0.25 | 98.56 | b.d. | 0.03 | 0.01 | 0.02 | b.d. | 98.87 |
| LNG3-11-1011 | 0.01 | 0.14 | 99.09 | 0.01 | b.d. | 0.01 | b.d. | 0.03 | 99.29 |
| LNG3-11-1012 | b.d. | 0.1 | 98.25 | b.d. | b.d. | 0.01 | b.d. | 0.02 | 98.38 |
| LNG3-11-1013 | b.d. | 0.29 | 99.34 | b.d. | 0.01 | b.d. | 0.01 | b.d. | 99.64 |
| LNG3-11-1014 | 0.02 | 0.25 | 100.57 | 0.01 | b.d. | 0.02 | b.d. | 0.01 | 100.87 |
| LNG3-11-1021 | b.d. | 0.07 | 99.78 | 0.01 | b.d. | b.d. | b.d. | 0.02 | 99.89 |
| LNG3-11-1022 | b.d. | 0.36 | 99.13 | b.d. | b.d. | b.d. | b.d. | 0.01 | 99.5 |
| LNG3-11-1023 | b.d. | 0.29 | 98.94 | 0.01 | b.d. | 0.01 | b.d. | 0.01 | 99.26 |
| LNG3-11-1024 | b.d. | 0.27 | 99.55 | b.d. | b.d. | b.d. | b.d. | b.d. | 99.82 |
| LNG3-11-1025 | b.d. | 0.18 | 99.13 | b.d. | 0.01 | 0.02 | 0.01 | b.d. | 99.36 |
| LNG3-11-1026 | b.d. | 0.17 | 98.82 | b.d. | b.d. | b.d. | b.d. | 0.01 | 99 |
| LNG3-11-2011 | b.d. | 0.31 | 99.12 | b.d. | b.d. | 0.01 | 0.01 | 0.02 | 99.48 |
| LNG3-11-2012 | b.d. | 0.27 | 99.02 | 0.01 | b.d. | b.d. | b.d. | 0.02 | 99.32 |
| LNG3-11-2013 | b.d. | 0.27 | 99.42 | b.d. | 0.02 | 0.02 | 0.02 | b.d. | 99.76 |
| LNG3-11-2014 | 0.01 | 0.27 | 98.85 | b.d. | b.d. | b.d. | 0.01 | b.d. | 99.13 |
| LNG3-11-3011 | b.d. | 0.05 | 98.76 | 0.02 | b.d. | 0.01 | 0.01 | b.d. | 98.86 |
| LNG3-11-3012 | b.d. | 0.14 | 99.2 | b.d. | 0.03 | b.d. | 0.02 | 0.03 | 99.41 |
| LNG3-11-3013 | b.d. | 0.19 | 98.75 | b.d. | b.d. | b.d. | 0.01 | b.d. | 98.96 |
| LNG3-11-4011 | 0.01 | 0.11 | 99.29 | 0.01 | 0.01 | 0.01 | b.d. | 0.03 | 99.47 |
| LNG3-11-4012 | b.d. | 0.21 | 98.56 | 0.01 | 0.02 | b.d. | b.d. | 0.02 | 98.81 |
| LNG3-11-4013 | 0.01 | 0.17 | 98.34 | 0.01 | b.d. | 0.01 | b.d. | 0.02 | 98.55 |
| LNG3-11-4014 | b.d. | 0.15 | 98.39 | b.d. | 0.01 | b.d. | 0.01 | 0.04 | 98.58 |
| LNG3-11-5011 | b.d. | 0.29 | 98.69 | 0.01 | b.d. | 0.01 | b.d. | 0.08 | 99.09 |
| LNG3-11-5012 | 0.01 | 0.27 | 98.66 | 0.01 | b.d. | 0.02 | b.d. | b.d. | 98.97 |
| LNG3-11-5013 | 0.01 | 0.22 | 97.74 | b.d. | 0.02 | 0.01 | 0.01 | b.d. | 98.02 |
| LNG3-11-5014 | 0.01 | 0.17 | 98.94 | b.d. | 0.01 | 0.02 | b.d. | 0.01 | 99.16 |
| LNG3-11-5015 | 0.01 | 0.01 | 100.18 | 0.01 | 0.01 | 0.02 | b.d. | 0.03 | 100.27 |

**Appendix II. Trace elements content of quartz by LA-ICPMS. b.d. = below detect limit**

| Sample | | Li (ppm) | Be (ppm) | Al (ppm) | P (ppm) | K (ppm) | Ti (ppm) | Ge (ppm) |
|---|---|---|---|---|---|---|---|---|
| 3-11-1-a1 | Quartz I | 1 | b.d. | 110 | 4 | 1 | 76.2 | 1.7 |
| 3-11-1-a3 | Quartz I | b.d. | b.d. | 40 | 11 | 13 | 6.8 | 2.1 |
| 3-11-2-a2 | Quartz I | 1 | b.d. | 139 | 3 | 33 | 27.8 | 2.4 |

| | | | | | | | | |
|---|---|---|---|---|---|---|---|---|
| 3-1-1-a1 | Quartz I | 4 | b.d. | 251 | 5 | 13 | 68.7 | 1.4 |
| 3-12-1-a1 | Quartz I | b.d. | b.d. | 45 | 7 | b.d. | 30.8 | 1.3 |
| 3-6-1-a2 | Quartz I | 2 | b.d. | 113 | 7 | b.d. | 42 | 1 |
| 3-9-1-a4 | Quartz I | 2 | 0.1 | 247 | 6 | 37 | 32.4 | 1.9 |
| 3-9-2-a1 | Quartz I | b.d. | b.d. | 290 | 8 | 211 | 147 | 1.6 |
| 6-1-1-a1 | Quartz I | 2 | 0.1 | 297 | 9 | 26 | 36.2 | 1.7 |
| 6-1-1-a2 | Quartz I | 1 | b.d. | 90 | 7 | 4 | 33.8 | 1.3 |
| 6-1-1-a3 | Quartz I | 1 | 0.1 | 124 | 6 | b.d. | 35.9 | 1.7 |
| 3-11-1-b2 | Quartz II | b.d. | b.d. | 28 | 4 | 1 | 2.2 | 1.4 |
| 3-11-1-b2 | Quartz II | b.d. | b.d. | 15 | 14 | 20 | 26.9 | 1.4 |
| 3-11-1-b3 | Quartz II | b.d. | b.d. | 85 | 3 | 9 | 5.1 | 0.1 |
| 3-11-2-b3 | Quartz II | b.d. | b.d. | 96 | 14 | b.d. | 86.3 | 2 |
| 3-11-3-b2 | Quartz II | b.d. | b.d. | 30 | 3 | b.d. | 5.6 | 3.4 |
| 3-11-3-b3 | Quartz II | b.d. | b.d. | 9 | 1 | b.d. | 1.5 | 2 |
| 3-6-1-b1 | Quartz II | 10 | 0.5 | 480 | 8 | 42 | 6.6 | 3.3 |
| 3-6-1-b4 | Quartz II | 18 | 0.5 | 776 | 10 | 97 | 15.9 | 5.2 |
| 3-9-1-b2 | Quartz II | b.d. | b.d. | 14 | 8 | b.d. | 68.3 | 1.7 |
| 6-1-1-b4 | Quartz II | 1 | b.d. | 63 | 7 | b.d. | 1.5 | 1.6 |
| 3-11-1-c1 | Quartz III | 62 | b.d. | 1341 | 11 | b.d. | 1.6 | 3.9 |
| 3-11-1-c2 | Quartz III | 71 | b.d. | 1488 | 5 | 20 | 1.6 | 4 |
| 3-11-1-c3 | Quartz III | 18 | b.d. | 535 | 1 | 6 | 1.6 | 2 |
| 3-11-1-c4 | Quartz III | 35 | b.d. | 832 | 2 | 2 | 1.6 | 0.5 |
| 3-11-2-c1 | Quartz III | 27 | b.d. | 736 | 7 | 63 | 0.7 | 2.3 |
| 3-11-2-c2 | Quartz III | 53 | b.d. | 1206 | 21 | 20 | 1.5 | 3.4 |
| 3-11-2-c2 | Quartz III | 61 | b.d. | 1506 | 8 | 47 | 1.6 | 3.6 |
| 3-11-2-c4 | Quartz III | 69 | b.d. | 1535 | b.d. | 18 | 2.1 | 3.9 |
| 3-11-3-c1 | Quartz III | 29 | b.d. | 779 | 3 | 39 | 1.3 | 1.8 |
| 3-11-3-c3 | Quartz III | 36 | b.d. | 972 | 5 | b.d. | 0.8 | 1.9 |
| 3-1-1-c1 | Quartz III | 48 | b.d. | 1555 | 9 | 3 | 1.7 | 6.4 |
| 3-9-1-c2 | Quartz III | 61 | b.d. | 1175 | 8 | 4 | 1.3 | 2.1 |
| 3-9-2-c3 | Quartz III | 17 | b.d. | 597 | 7 | 7 | 1 | 2.6 |
| 3-11-2-d1 | Quartz IV | 59 | b.d. | 1301 | 8 | b.d. | 1.5 | 4 |
| 3-11-2-d2 | Quartz IV | 32 | b.d. | 750 | 13 | 20 | 1.8 | 2.1 |
| 3-12-1-d1 | Quartz IV | 56 | b.d. | 1508 | 7 | 15 | 2 | 3.9 |
| 3-12-1-d2 | Quartz IV | 117 | b.d. | 2439 | 7 | 24 | 2.9 | 5.7 |
| 3-6-1-d1 | Quartz IV | 60 | b.d. | 1759 | 8 | b.d. | 1.9 | 28.8 |
| 3-6-1-d3 | Quartz IV | 69 | b.d. | 1534 | 4 | 54 | 1.3 | 17.8 |
| 3-9-2-d1 | Quartz IV | 64 | b.d. | 1142 | 7 | 23 | 1.2 | 3.3 |
| 3-9-2-d2 | Quartz IV | 45 | b.d. | 1152 | 6 | 1 | 1.4 | 2.5 |

## Appendix III. SHRIMP oxygen isotope of quartz and fluids

| Sample | 18O/16O | 95%T_err | ¦Ä18¦¯VSMOW(¡ë) | Error | External error | |
|---|---|---|---|---|---|---|
| 3-11-1-a1 | 0.002016 | 4.19E-07 | 8.6 | 0.21 | 0.45 | Quartz I |
| 3-11-1-a2 | 0.002019 | 6.95E-07 | 10 | 0.34 | 0.53 | Quartz I |
| 3-11-1-a3 | 0.002021 | 4.29E-07 | 10.9 | 0.21 | 0.45 | Quartz I |
| 3-11-2-a1 | 0.002019 | 5.79E-07 | 10 | 0.29 | 0.49 | Quartz I |
| 3-11-2-a2 | 0.002016 | 3.87E-07 | 8.4 | 0.19 | 0.44 | Quartz I |
| 3-11-3-a1 | 0.002031 | 3.22E-07 | 15.7 | 0.16 | 0.43 | Quartz I |
| 3-11-3-a2 | 0.00202 | 3.21E-07 | 10.4 | 0.16 | 0.43 | Quartz I |
| 3-1-1-a1 | 0.002026 | 3.05E-07 | 13.2 | 0.15 | 0.43 | Quartz I |
| 3-1-1-a2 | 0.002033 | 4.15E-07 | 16.8 | 0.2 | 0.45 | Quartz I |
| 3-1-1-a3 | 0.002022 | 2.81E-07 | 11.3 | 0.14 | 0.42 | Quartz I |
| 3-12-1-a1 | 0.002026 | 3.33E-07 | 13.6 | 0.16 | 0.43 | Quartz I |
| 3-12-1-a2 | 0.002027 | 2.45E-07 | 14 | 0.12 | 0.42 | Quartz I |
| 3-12-1-a3 | 0.00202 | 2.73E-07 | 10.3 | 0.14 | 0.42 | Quartz I |
| 3-6-1-a2 | 0.00202 | 4.07E-07 | 10.5 | 0.2 | 0.45 | Quartz I |
| 3-9-1-a1 | 0.002033 | 3.76E-07 | 16.6 | 0.18 | 0.44 | Quartz I |
| 3-9-1-a2 | 0.002027 | 4.05E-07 | 14.1 | 0.2 | 0.45 | Quartz I |
| 3-9-1-a2 | 0.002029 | 3.25E-07 | 14.8 | 0.16 | 0.43 | Quartz I |
| 3-9-1-a3 | 0.002025 | 3.58E-07 | 12.8 | 0.18 | 0.44 | Quartz I |
| 3-9-1-a4 | 0.002022 | 3.55E-07 | 11.4 | 0.18 | 0.44 | Quartz I |
| 3-9-2-a1 | 0.002029 | 3.64E-07 | 14.9 | 0.18 | 0.44 | Quartz I |
| 3-9-2-a2 | 0.002025 | 4.19E-07 | 12.9 | 0.21 | 0.45 | Quartz I |
| 3-9-2-a3 | 0.002018 | 3.43E-07 | 9.6 | 0.17 | 0.43 | Quartz I |
| 6-1-1-a1 | 0.002032 | 3.77E-07 | 16.2 | 0.19 | 0.44 | Quartz I |
| 6-1-1-a2 | 0.002023 | 4.29E-07 | 12 | 0.21 | 0.45 | Quartz I |
| 6-1-1-a3 | 0.002027 | 4.41E-07 | 14 | 0.22 | 0.46 | Quartz I |
| 6-1-1-a4 | 0.002026 | 4.26E-07 | 13.3 | 0.21 | 0.45 | Quartz I |

| Fluid 250¡æ | | | | | | | |
|---|---|---|---|---|---|---|---|
| 3-11-1-b1 | 0.002033 | 5.22E-07 | 16.7 | 0.26 | 0.48 | Quartz II | 7.8 |
| 3-11-1-b2 | 0.002029 | 3.96E-07 | 15.1 | 0.2 | 0.45 | Quartz II | 6.2 |
| 3-11-1-b3 | 0.002023 | 4.25E-07 | 12.1 | 0.21 | 0.45 | Quartz II | 3.2 |
| 3-11-1-b4 | 0.002027 | 4.77E-07 | 13.9 | 0.24 | 0.46 | Quartz II | 5 |

| | | | | | | | |
|---|---|---|---|---|---|---|---|
| 3-11-2-b1 | 0.002032 | 4.56E-07 | 16.2 | 0.22 | 0.46 | Quartz II | 7.3 |
| 3-11-2-b2 | 0.002033 | 6.31E-07 | 16.8 | 0.31 | 0.51 | Quartz II | 8 |
| 3-11-3-b1 | 0.002035 | 2.04E-07 | 18 | 0.1 | 0.41 | Quartz II | 9.1 |
| 3-11-3-b2 | 0.002029 | 3.3E-07 | 14.8 | 0.16 | 0.43 | Quartz II | 5.9 |
| 3-11-3-b3 | 0.002026 | 2.7E-07 | 13.6 | 0.13 | 0.42 | Quartz II | 4.7 |
| 3-1-1-b1 | 0.002049 | 3.39E-07 | 24.8 | 0.17 | 0.43 | Quartz II | 15.9 |
| 3-1-1-b2 | 0.002046 | 2.43E-07 | 23 | 0.12 | 0.42 | Quartz II | 14.2 |
| 3-1-1-b3 | 0.002036 | 3.59E-07 | 18.3 | 0.18 | 0.44 | Quartz II | 9.4 |
| 3-1-1-b4 | 0.00204 | 4.08E-07 | 20.3 | 0.2 | 0.45 | Quartz II | 11.4 |
| 3-12-1-b2 | 0.002032 | 3.79E-07 | 16.3 | 0.19 | 0.44 | Quartz II | 7.4 |
| 3-12-1-b3 | 0.002027 | 3.03E-07 | 13.7 | 0.15 | 0.43 | Quartz II | 4.8 |
| 3-6-1-b1 | 0.00203 | 3.46E-07 | 15.3 | 0.17 | 0.43 | Quartz II | 6.4 |
| 3-6-1-b2 | 0.002032 | 4.45E-07 | 16.4 | 0.22 | 0.46 | Quartz II | 7.5 |
| 3-6-1-b3 | 0.002029 | 3.72E-07 | 15 | 0.18 | 0.44 | Quartz II | 6.1 |
| 3-6-1-b4 | 0.002035 | 3.16E-07 | 17.6 | 0.16 | 0.43 | Quartz II | 8.7 |
| 3-9-1-b1 | 0.002031 | 3.77E-07 | 15.9 | 0.19 | 0.44 | Quartz II | 7 |
| 3-9-1-b2 | 0.002026 | 3.52E-07 | 13.4 | 0.17 | 0.44 | Quartz II | 4.5 |
| 3-9-1-b3 | 0.002043 | 4.22E-07 | 22 | 0.21 | 0.45 | Quartz II | 13.1 |
| 3-9-1-b4 | 0.002037 | 4.36E-07 | 18.7 | 0.21 | 0.45 | Quartz II | 9.8 |
| 3-9-2-b1 | 0.002025 | 3.35E-07 | 12.8 | 0.17 | 0.43 | Quartz II | 3.9 |
| 3-9-2-b2 | 0.002035 | 4E-07 | 17.8 | 0.2 | 0.45 | Quartz II | 8.9 |
| 3-9-2-b3 | 0.002041 | 5.16E-07 | 21 | 0.25 | 0.47 | Quartz II | 12.1 |
| 6-1-1-b1 | 0.002041 | 6.13E-07 | 20.7 | 0.3 | 0.5 | Quartz II | 11.8 |
| 6-1-1-b2 | 0.002046 | 4.86E-07 | 23.1 | 0.24 | 0.47 | Quartz II | 14.2 |
| 6-1-1-b31 | 0.002038 | 3.71E-07 | 19.2 | 0.18 | 0.44 | Quartz II | 10.3 |
| 6-1-1-b4 | 0.00203 | 3.45E-07 | 15.2 | 0.17 | 0.43 | Quartz II | 6.3 |
| 6-1-1-b51 | 0.002032 | 3.9E-07 | 16.3 | 0.19 | 0.44 | Quartz II | 7.4 |
| 6-1-1-b6 | 0.002036 | 3.73E-07 | 18.1 | 0.18 | 0.44 | Quartz II | 9.2 |
| Fluid 200¡æ | | | | | | | |
| 3-11-1-c1 | 0.002049 | 4.09E-07 | 24.5 | 0.2 | 0.45 | Quartz III | 12.9 |
| 3-11-1-c2 | 0.002049 | 3.96E-07 | 24.9 | 0.19 | 0.44 | Quartz III | 13.3 |
| 3-11-1-c3 | 0.002048 | 4.65E-07 | 24.1 | 0.23 | 0.46 | Quartz III | 12.5 |
| 3-11-1-c4 | 0.002049 | 4.53E-07 | 24.7 | 0.22 | 0.46 | Quartz III | 13.1 |
| 3-11-2-c1 | 0.002049 | 5.23E-07 | 24.6 | 0.26 | 0.47 | Quartz III | 13 |
| 3-11-2-c2 | 0.002049 | 4.65E-07 | 24.7 | 0.23 | 0.46 | Quartz III | 13.1 |
| 3-11-2-c2 | 0.002051 | 2.64E-07 | 25.9 | 0.13 | 0.42 | Quartz III | 14.3 |
| 3-11-2-c3 | 0.002049 | 4.56E-07 | 24.9 | 0.22 | 0.46 | Quartz III | 13.3 |
| 3-11-3-c1 | 0.002052 | 3.44E-07 | 26.2 | 0.17 | 0.43 | Quartz III | 14.6 |
| 3-11-3-c2 | 0.002051 | 3.02E-07 | 25.7 | 0.15 | 0.43 | Quartz III | 14.1 |
| 3-11-3-c3 | 0.002049 | 3.09E-07 | 24.9 | 0.15 | 0.43 | Quartz III | 13.3 |
| 3-1-1-c1 | 0.002055 | 2.98E-07 | 27.8 | 0.15 | 0.43 | Quartz III | 16.2 |
| 3-1-1-c2 | 0.002051 | 3.37E-07 | 25.8 | 0.16 | 0.43 | Quartz III | 14.2 |
| 3-1-1-c3 | 0.002051 | 2.63E-07 | 25.6 | 0.13 | 0.42 | Quartz III | 14 |
| 3-1-1-c4 | 0.00205 | 3.14E-07 | 25.5 | 0.15 | 0.43 | Quartz III | 13.9 |
| 3-9-1-c1 | 0.002053 | 3.18E-07 | 26.7 | 0.15 | 0.43 | Quartz III | 15.1 |
| 3-9-1-c2 | 0.002052 | 3.93E-07 | 26.4 | 0.19 | 0.44 | Quartz III | 14.8 |
| 3-9-1-c3 | 0.002054 | 3.83E-07 | 27.1 | 0.19 | 0.44 | Quartz III | 15.4 |
| 3-9-1-c4 | 0.002055 | 4.31E-07 | 27.5 | 0.21 | 0.45 | Quartz III | 15.9 |
| 3-9-2-c1 | 0.002053 | 4.45E-07 | 26.5 | 0.22 | 0.45 | Quartz III | 14.9 |
| 3-9-2-c2 | 0.002054 | 3.33E-07 | 27.2 | 0.16 | 0.43 | Quartz III | 15.6 |
| 3-9-2-c3 | 0.002049 | 3.57E-07 | 24.6 | 0.17 | 0.44 | Quartz III | 13 |
| Fluid 150¡æ | | | | | | | |
| 3-11-1-d1 | 0.002051 | 4.25E-07 | 25.7 | 0.21 | 0.45 | Quartz IV | 10.3 |
| 3-11-1-d2 | 0.002053 | 4.14E-07 | 26.9 | 0.2 | 0.45 | Quartz IV | 11.5 |
| 3-11-1-d3 | 0.002053 | 5.38E-07 | 26.6 | 0.26 | 0.48 | Quartz IV | 11.3 |
| 3-11-1-d4 | 0.002052 | 3.96E-07 | 26.1 | 0.19 | 0.44 | Quartz IV | 10.8 |
| 3-11-2-d1 | 0.002052 | 3.7E-07 | 26 | 0.18 | 0.44 | Quartz IV | 10.7 |
| 3-11-2-d2 | 0.002052 | 3.33E-07 | 26.4 | 0.16 | 0.43 | Quartz IV | 11 |
| 3-12-1-d1 | 0.00205 | 3.46E-07 | 25.3 | 0.17 | 0.43 | Quartz IV | 9.9 |
| 3-12-1-d2 | 0.00205 | 3.83E-07 | 25.2 | 0.19 | 0.44 | Quartz IV | 9.9 |
| 3-12-1-d3 | 0.002049 | 2.82E-07 | 24.8 | 0.14 | 0.42 | Quartz IV | 9.5 |
| 3-6-1-d1 | 0.002053 | 4.11E-07 | 26.6 | 0.2 | 0.45 | Quartz IV | 11.2 |
| 3-6-1-d2 | 0.002053 | 4.03E-07 | 26.6 | 0.2 | 0.45 | Quartz IV | 11.2 |
| 3-6-1-d3 | 0.002053 | 3.81E-07 | 26.5 | 0.19 | 0.44 | Quartz IV | 11.2 |
| 3-6-1-d4 | 0.002053 | 3.1E-07 | 26.8 | 0.15 | 0.43 | Quartz IV | 11.5 |
| 3-9-2-d1 | 0.002049 | 3.39E-07 | 24.9 | 0.17 | 0.43 | Quartz IV | 9.6 |
| 3-9-2-d2 | 0.002048 | 3.83E-07 | 24.3 | 0.19 | 0.44 | Quartz IV | 9 |
| 3-9-2-d3 | 0.00205 | 3.2E-07 | 25.2 | 0.16 | 0.43 | Quartz IV | 9.9 |

## References


Ackerson, M.R., Tailby, N.D., Watson, E.B., 2015. Trace elements in quartz shed light on sediment provenance. Geochem. Geophys. Geosyst. 18 (9), 1687–2023.

Alexandre, A., Basile-Doelsch, I., Sonzogni, C., Sylvestre, F., Parron, C., Meunier, J.D., Colin, F., 2006. Oxygen isotope analyses of fine silica grains using laser-extraction technique: comparison with oxygen isotope data obtained from ion microprobe analyses and application to quartzite and silcrete cement investigation. Geochim. Cosmochim. Acta 70, 2827–2835.

Arehart, G.B., 1996. Characteristics and origin of sediment-hosted disseminated gold deposits: a review. Ore Geol. Rev. 11 (6), 383–403.

Audetat, A., Garbe-Schonberg, D., Kronz, A., Pettke, T., Rusk, B., Donovan, J.J., Lowers, H.A., 2015. Characterisation of a natural quartz crystal as a reference material for microanalytical determination of Ti, Al, Li, Fe, Mn, Ga and Ge. Geostand. Geoanal. Res. 39, 171–184.

Breiter, K., Ackerman, L., Svojtka, M., Muller, A., 2013. Behavior of trace elements in quartz from plutons of different geochemical signature: a case study from the Bohemian Massif, Czech Republic. Lithos 175–176, 54–67.
Chen, M.H., Mao, J.W., Frank, P.B., Norman, T., Uttley, P., 2011. Structural features and metallogenesis of the Carlin-type Jinfeng (Lannigou) gold deposit, Guizhou Province, China. Ore Geol. Rev. 43, 217–234.
Chen, M.H., Mao, J.W., Li, C., Zhang, Z.Q., Dang, Y., 2015a. Re-Os isochron ages for arsenopyrite from Carlin-like gold deposits in the Yunnan–Guizhou–Guangxi "golden triangle", southwestern China. Ore Geol. Rev. 64, 316–327.
Chen, M.H., Zhang, Z.Q., Santosh, M., Dang, Y., Zhang, W., 2015b. The Carlin-type gold deposits of the "golden triangle" of SW China: Pb and S isotopic constraints for the ore genesis. J. Asian Earth Sci. 103, 115–128.
Chenery, S., Cook, J., 1993. Determination of rare earth elements in single mineral grains by laser ablation microprobe-inductively coupled plasma mass spectrometry—preliminary study. J. Anal Atom Spectrum 8, 299–303.
Clayton, R.N., Mayeda, T.K., Oneil, J.R., 1972. Oxygen isotope-exchange between quartz and water. J. Geophys. Res. 77, 3057–3067.
Cline, J.S., Hofstra, A.H., 2000. Ore-fluid evolution at the Getchell Carlin-type gold deposit, Nevada, USA. Eur. J. Mineral. 12 (1), 195–212.
Cline, J.S., Hofstra, A.H., Muntean, J.L., Tosdal, R.M., Hickey, K.A., 2005. Carlin-Type gold deposits in Nevada: critical geologic characteristics and viable models. Econ. Geol. 100th Anniversary Volume 451–484.
Cathodoluminescence and its application to geoscience. In: Coulson, I.M. (Ed.), Mineralogical Association of Canada Short Course. 45 (182 p).
Dobra, J.L., 1997. The US gold industry 1996. In: Nevada Bureau of Mines and Geology, Special Publication 21.
Gold Corp, Eldorado, Eldorado Gold Corp. Ltd., 2011. Technical Report for the Jinfeng Gold Mine, China.
Gotte, T., Pettke, T., Ramseyer, K., Koch-Müller, M., Mullis, J., 2011. Cathodo-luminescence properties and trace element signature of hydrothermal quartz: a fingerprint of growth dynamics. Amer. Miner. 96, 802–813.
Hofstra, A.H., Cline, J.S., 2000. Characteristics and models for Carlin-type gold deposits. In: Hagemann, S.G., Brown, P.E. (Eds.), Gold in 2000: Rev. Econ. Geol. 13. pp. 163–220.
Hofstra, A.H., Snee, L.W., Rye, R.O., Folger, H.W., Phinisey, J.D., Loranger, R.J., Dahl, A.R., Naeser, C.W., Stein, H.J., Lewchuk, M., 1999. Age constraints on Jerritt Canyon and other Carlin-type gold deposits in the western United States – relation to mid-Tertiary extension and magmatism. Econ. Geol. 94, 769–802.
Hofstra, A.H., Emsbo, P., Christiansen, W.D., Theodorakos, P., Zhang, X.C., Hu, R.Z., Su, W.C., Fu, S.H., 2005. Source of ore fluids in Carlin-type gold deposits, China: Implications for genetic models. In: Miner. Deposit Research 8th Biennial SGA Meeting, Beijing.
Hu, R.Z., Zhou, M.F., 2012. Multiple Mesozoic mineralization events in South China-an introduction to the thematic issue. Mineral. Deposita 47, 579–588.
Hu, R.Z., Su, W.C., Bi, X.W., Tu, G.Z., Hofstra, A.H., 2002. Geology and geochemistry of Carlin-type gold deposits in China. Mineral. Deposita 37 (3–4), 378–392.
Hu, R.Z., Fu, S.L., Xiao, J.F., 2016. Major scientific problems on low-temperature metallogenesis in South China. Acta Petrol. Sin. 32, 3239–3251 (in Chinese with English abstract).
Hu, R.Z., Fu, S.L., Huang, Y., Zhou, M.F., Fu, S.H., Zhao, C.H., Wang, Y.J., Bi, X.W., Xiao, J.F., 2017. The giant South China Mesozoic low-temperature metallogenic domain-reviews and a new geodynamic model. J. Asian Earth Sci. 137, 9–34.
Ickert, R.B., Hiess, J., Williams, I.S., Holden, P., Ireland, T.R., Lanc, P., Schram, N., Foster, J.J., Clement, S.W., 2008. Determining high precision, in situ, oxygen isotope ratios with a SHRIMP II: analyses of MPI-DING silicate-glass reference materials and zircon from contrasting granites. Chem. Geol. 257, 114–128.
Landtwing, M., Pettke, T., 2005. Relationships between SEM-cathodoluminescence response and trace element composition of hydrothermal vein quartz. Am. Mineral. 90, 122–131.
Lehmann, K., Pettke, T., Ramseyer, K., 2011. Significance of trace elements in syntaxial quartz cement, Haushi Group sandstones, Sultanate of Oman. Chem. Geol. 280, 47–57.
Liu, J.Z., Yang, C.F., Wang, Z.P., 2017. Geological feature of Shuiyindong Carlin-type gold deposit, Guizhou, China. Geol. Surv. China 4 (2), 32–41 2017. (in Chinese with English abstract).
Lubben, J.D., Cline, J.S., Barker, S., 2012. Ore fluid properties and sources from quartz-associated gold at the Betze-post Carlin-type gold deposit, Nevada, United States. Econ. Geol. 107, 1351–1385.
Mao, J.W., Cheng, Y.B., Chen, M.H., Pirajno, F., 2013. Major types and time- space distribution of Mesozoic ore deposits in South China and their geodynamic settings. Mineral. Deposita 48, 267–294.
Mao, W., Rusk, B., Yang, F.C., Zhang, M.J., 2017. Physical and chemical evolution of the Dabaoshan porphyry Mo deposit, south China: insights from fluid inclusions, cathodoluminescence, and trace elements in quartz. Econ. Geol. 112, 889–918.
Matsuhisa, Y., Goldsmith, J.R., Clayton, R.N., 1979. Oxygen isotopic fractionation in the system quartz-albite-anorthite-water. Geochim. Cosmochim. Acta 1979 (43), 1131–1140.
Müller, A., Wiedenbeck, M., Van den Kerkhoff, A.M., Kronz, A., Simon, K., 2003. Trace elements in quartz–a combined electron microprobe, secondary ion mass spectrometry, laser-ablation ICP-MS, and cathodoluminescence study. Eur. J. Mineral. 15, 747–763.
Muntean, J.L., Cline, J.S., 2018. Diversity of Carlin-style gold deposits. Rev. Econ. Geol. 20, 1–6.
Muntean, J.L., Cline, J.S., Simon, A.C., Longo, A.A., 2011. Magmatic–hydrothermal origin of Nevada's Carlin-type gold deposits. Nat. Geosci. 4 (2), 12–127.
Murray, M.A., Bruce, Y., 2007. Tracking meteoric infiltration into a magmatic-hydrothermal system: a cathodoluminescence, oxygen isotope and trace element study of quartz from Mt. Leyshon, Australia. Chem. Geol. 240, 343–360.
Paton, C., Hellstrom, J., Paul, B., Woodhead, J., Hergt, J., 2011. Iolite: freeware for the visualisation and processing of mass spectrometric data. J. Analytic. Atom. Spectrom. 26 (12), 2508–2518.
Peters, S.G., Huang, J.Z., Li, Z.P., Jing, C.G., 2007. Sedimentary rock-hosted au deposits of the Dian–Qian–Gui area. Ore Geol. Rev. 31, 170–204.
Pi, Q.H., Hu, R.Z., Xiong, B., Li, Q.L., Zhong, R.C., 2017. In situ SIMS U-Pb dating of hydrothermal rutile: reliable age for the Zhesang Carlin-type gold deposit in the golden triangle region, SW China. Mineral. Deposita 52 (8), 1179–1190.
Rusk, B.G., 2014. Chapter 7. Quartz cathodoluminescence: textures, trace elements, and geological applications. 2014 In: Coulson, I.M. (Ed.), Cathodoluminescence and Its Application to Geoscience. Mineralogical Association of Canada Short Course. 45. pp. 127–141.
Rusk, B.G., Lowers, H.A., Reed, M.H., 2008. Trace elements in hydrothermal quartz: Relationships to cathodoluminescent textures and insights into vein formation. Geology 36 (7), 547–550.
Su, W.C., Heinrich, C.A., Pettke, T., Zhang, X.C., Hu, R.Z., Xia, B., 2009a. Sediment-hosted gold deposits in Guizhou, China: products of wall-rock sulfidation by deep crustal fluids. Econ. Geol. 104, 73–93.
Su, W.C., Hu, R.Z., Xia, B., Xia, Y., Liu, Y.P., 2009b. Calcite Sm-Nd isochron age of the Shuiyindong Carlin-type gold deposit, Guizhou, China. Chem. Geol. 258, 269–274.
Su, W.C., Xia, B., Zhang, H.T., Zhang, X.C., Hu, R.Z., 2008. Visible gold in arsenian pyrite at the Shuiyindong Carlin-type gold deposit, Guizhou, China: implications for the environment and processes of ore formation. Ore Geol. Rev. 33, 667–679.
Su, W.C., Zhang, H.T., Hu, R.Z., Ge, X., Xia, B., Chen, Y.Y., Zhu, C., 2012. Mineralogy and geochemistry of gold-bearing arsenian pyrite from the Shuiyindong Carlin-type gold deposit, Guizhou, China: implications for gold depositional processes. Mineral. Deposita 47, 653–662.
Su, W.C., Dong, W.D., Zhang, X.C., Shen, N.P., Hu, R.Z., Hofstra, A.H., Cheng, L.Z., Xia, Y., Yang, K.Y., 2018. Carlin-type gold deposits in the Dian-Qian-Gui "Golden Triangle" of southwest China. Rev. Econ. Geol. 20, 157–185.
Tan, Q.P., Xia, Y., Xie, Z.J., Yan, J., Wei, D.T., 2015. S, C, O, H, and Pb isotopic studies for the Shuiyindong Carlin-type gold deposit, southwest Guizhou, China: constraints for ore genesis. Chin. J. Geochem. 93, 525–539.
Tanner, D., Henley, R.W., Mavrogenes, J.A., Holden, P., 2013. Combining in situ isotopic, trace element and textural analyses of quartz from four magmatic-hydrothermal ore deposits. Contrib. Mineral. Petrol. 166 (4), 1119–1142.
Tu, G., 1992. Some problems on prospecting of super large gold deposits. Acta Geol Sichuan Spec Issue 12, 1–9 (in Chinese).
Wang, G.Z., Hu, R.Z., Su, W.C., Zhu, L.M., 2003. Fluid flow and mineralization of Youjiang Basin in the Yunnan-Guizhou-Guangxi area, China. Sci. in China (Series D) 46, 99–109.
Wang, Y.J., Fan, W.M., Sun, M., Liang, X.Q., Zhang, Y.H., Peng, T.P., 2007. Geochronological, geochemical and geothermal constraints on petrogenesis of the Indosinian peraluminous granites in the south China block: a case study in the Hunan Province. Lithos 96, 475–502.
Xie, Z.J., Xia, Y., Cline, J.S., Pribil, M.J., Koenig, A., Tan, Q.P., Wei, D.T., Wang, Z.P., Yan, J., 2018. Magmatic origin for sediment-hosted Au deposits, Guizhou province, China: in situ chemistry and sulfur isotope composition of pyrites, Shuiyindong and Jinfeng deposits. Econ. Geol. 113 (7), 1627–1652.
Yan, J., Hu, R.Z., Liu, S., Lin, Y.T., Zhang, J.C., Fu, S.L., 2018. NanoSIMS element mapping and sulfur isotope analysis of Au-bearing pyrite from Lannigou Carlin-type Au deposit in SW China: new insights into the origin and evolution of Au-bearing fluids. Ore Geol. Rev. 92, 29–41.
Zhang, X.C., Spiro, B., Halls, C., Stanley, C.J., Yang, K.Y., 2003. Sediment-hosted disseminated gold deposits in southwest Guizhou, PRC: their geological setting and origin in relation to mineralogical, fluid inclusion, and stable-isotope characteristics. Int. Geol. Rev. 45, 407–470.
Zhou, X.M., Sun, T., Shen, W.Z., Shu, L.S., Niu, Y.L., 2006. Petrogenesis of Mesozoic granitoids and volcanic rocks in south China: a response to tectonic evolution. Episodes 29, 26–33.
Zhu, J.J., Hu, R.Z., Richards, J.P., Bi, X.W., Stern, R., Lu, G., 2017. No genetic link between Late Cretaceous felsic dikes and Carlin-type Au deposits in the Youjiang basin, southwest China. Ore Geol. Rev. 84, 328–337.